

# LJMU Research Online

Liu, Q, Huang, H, Iglesias, G, Wang, J and Bashir, M

Fully coupled aero-hydrodynamic analysis of floating vertical axis wind turbines in staggered configurations

https://researchonline.ljmu.ac.uk/id/eprint/27339/

# Article

**Citation** (please note it is advisable to refer to the publisher's version if you intend to cite from this work)

Liu, Q ORCID logoORCID: https://orcid.org/0009-0001-1925-652X, Huang, H, Iglesias, G ORCID logoORCID: https://orcid.org/0000-0003-2719-1663, Wang, J ORCID logoORCID: https://orcid.org/0000-0003-4646-9106 and Bashir, M ORCID logoORCID: https://orcid.org/0000-0002-4331-4275 (2025) Fully

LJMU has developed LJMU Research Online for users to access the research output of the University more effectively. Copyright © and Moral Rights for the papers on this site are retained by the individual authors and/or other copyright owners. Users may download and/or print one copy of any article(s) in LJMU Research Online to facilitate their private study or for non-commercial research. You may not engage in further distribution of the material or use it for any profit-making activities or any commercial gain.

The version presented here may differ from the published version or from the version of the record. Please see the repository URL above for details on accessing the published version and note that access may require a subscription.

For more information please contact <a href="mailto:researchonline@ljmu.ac.uk">researchonline@ljmu.ac.uk</a>



Contents lists available at ScienceDirect

# Energy

journal homepage: www.elsevier.com/locate/energy



# Fully coupled aero-hydrodynamic analysis of floating vertical axis wind turbines in staggered configurations

Qingsong Liu<sup>a</sup>, Haoda Huang<sup>b</sup>, Gregorio Iglesias<sup>c,d</sup>, Jin Wang<sup>e</sup>, Musa Bashir<sup>a,\*</sup>

- <sup>a</sup> School of Engineering, University of Liverpool, The Quadrangle, Brownlow Hill, L69 3GH, United Kingdom
- <sup>b</sup> School of Energy and Power Engineering, University of Shanghai for Science and Technology, Shanghai, 200093, China
- c School of Engineering, Computing and Mathematics (SECaM), University of Plymouth, Plymouth, PL48 AA, United Kingdom
- <sup>d</sup> School of Engineering and Architecture, University College Cork, Ireland, T12 K8AF, United Kingdom
- <sup>e</sup> Liverpool Logistics, Offshore and Marine (LOOM) Research Institute, Liverpool John Moores University, Byrom Street, Liverpool, L3 3AF, United Kingdom

#### ARTICLE INFO

### Keywords:

Floating vertical axis wind turbine (VAWT) Wind farm layout optimization Computational fluid dynamics (CFD) Offshore wind energy

#### ABSTRACT

Floating vertical axis wind turbines (VAWTs) present a promising alternative to traditional horizontal axis wind turbines (HAWTs), offering higher power density and potential reductions levelized cost of electricity (LCOE). However, the performance of floating VAWT arrays in real world marine environments remains poorly understood, hindering their commercial viability. This study introduces a novel, fully coupled aero-hydrodynamic simulation framework, based on dynamic fluid-body interaction (DFBI) theory, to resolve the complex interaction between aerodynamic wake interactions, platform motion, and hydrodynamic loads in staggered floating VAWT configurations. The framework integrates orthogonal experimental design (OED) to systematically evaluate key layout parameters (turbine spacing, inflow angle, and rotational direction) for staggered bottom-fixed VAWT arrays. The inflow angle emerges as the dominant factor, with optimized staggered configurations achieving a 5 % increase in power density over isolated turbines. Comparative analysis of tandem, parallel, and staggered configurations demonstrates that staggered arrays uniquely mitigate wake interference through enhanced flow channeling and accelerated wake recovery, outperforming tandem layouts (which suffer up to 11.8 % efficiency losses) and parallel arrangements (limited by spacing-dependent symmetry breakdown). For staggered floating systems, the framework incorporates six-degree-of-freedom platform motion, revealing that hydrodynamic-induced platform dynamics amplify performance indicator by 22 % compared to fixed-bottom counterparts. This synergistic coupling between aerodynamic wake effects and wave-driven platform oscillations highlights the necessity of holistic aero-hydrodynamic modelling for accurate performance predictions. The framework's predictive capabilities, validated against baseline cases, offer actionable insights for minimizing wake losses and maximizing energy yield in cost-sensitive marine environments. These advances position staggered floating VAWT arrays as a scalable, economically competitive solution for offshore wind energy expansion, directly addressing global decarbonization challenges.

# 1. Introduction

Wind energy is playing an increasingly important role in mitigating global warming, reducing environmental pollution, and addressing the energy crisis. In recent years, governments worldwide have launched ambitious policies to accelerate the energy transition, with a strong emphasis on the large-scale deployment of megawatt-class wind turbines both onshore and offshore. These initiatives have driven the rapid expansion of the global wind energy industry. According to the Global Wind Energy Council [1], 2024 was the wind industry's most successful

year to date, with 117 GW of new capacity added worldwide bringing total installed capacity to 1136 GW, an 11 % increase over the previous year. However, offshore wind installations declined to 8 GW, down 26 % year-on-year and marking the lowest level since 2021. This slowdown highlights the growing need for further research and technological innovation to overcome the challenges facing offshore wind development.

HAWTs have dominated the wind energy market for the past few decades. However, floating offshore wind farms in deep waters face significant challenges, including complex installation, stability issues

E-mail address: m.b.bashir@liverpool.ac.uk (M. Bashir).

<sup>\*</sup> Corresponding author.

due to deep water dynamics, and increased maintenance demands. Maintaining structural integrity and reducing the levelized cost of energy (LCOE) for floating HAWTs have become increasingly difficult due to the growing size of the blades and support structures needed to capture energy within the megawatt range and keep the turbines afloat. A prospective solution to these challenges can be found in floating VAWTs, which present advantages in terms of power density, directionality, and operations and maintenance (O&M) thanks to their reduced mechanical complexity and easier access to the generator and gearbox [2–4].

For conventional offshore HAWTs, more than 20 % of failures occur in components within the nacelle, such as the gearbox, generator, and yaw system [5-9], Additionally, the scarcity of specialized installation vessels required for maintenance at heights exceeding 100 m makes the system highly susceptible to downtime, leading to significant economic losses [10-12]. Compared to HAWTs, VAWTs feature a drivetrain installed at the base and do not require pitch and yaw control systems, making wind farm installation and maintenance more convenient in harsh offshore environments [13]. Moreover, the drivetrain of a VAWT can be entirely housed within the floating platform, enhancing platform stability and significantly reducing overturning moments. As a result, the floating structure required for stability in VAWTs can be smaller than that of HAWTs, offering a substantial cost advantage [14]. A study by Ennis et al. [15] from Sandia National Laboratories indicated that, due to lower equipment and maintenance expenses, the operational costs of offshore VAWTs can be 25 % lower than those of HAWTs with the same capacity, demonstrating a more pronounced economic benefit.

Beyond installation and cost considerations, VAWTs also demonstrate superior aerodynamic performance in wind farm arrays. In typical HAWT arrays, downstream turbines are highly susceptible to wake effects from upstream turbines, leading to energy losses. To mitigate wake interference, HAWTs typically require a spacing of 8-10 rotor diameters [16]. While this layout reduces wake effects, it also increases the land or sea area required, thereby lowering the power density of the wind farm. Dabiri's study [17] demonstrated that VAWT wake dissipates more rapidly than those of HAWTs. By optimizing turbine layouts within a wind farm, VAWTs can achieve a power density of 30 W/m<sup>2</sup>, which is 10-15 times higher than the standard 2-3 W/m<sup>2</sup> for HAWT-based wind farms [18]. This phenomenon has been validated by real-world power measurements from the "Windspire" wind farm. Further studies have also revealed mutual coupling effects between VAWTs [19], which not only enhance the power output of individual rotors but also accelerate wake recovery [20,21]. Experimental research by Vergaerde et al. [22] further confirmed that when two VAWTs are spaced approximately 1.3 times the rotor diameter and rotate in opposite directions, their wind energy utilization is 17 % higher than that of a single turbine. Some numerical simulations have also yielded similar conclusions [23,24]. When a cluster of VAWTs is arranged with counter-rotating turbines, the wake coupling effect significantly increases the power density per unit area [25-27].

### 1.1. Overview of layout parameters for VAWTs in an array

For a pair of VAWTs, the relative positioning can be characterized based on the rotation direction of each turbine (either co-rotating or counter-rotating), the incoming wind direction, and the relative layout angle  $\beta$  between the two turbines. As illustrated in Fig. 1, three typical arrangements are commonly considered:

- (a) Staggered layout: The second turbine is placed downstream with an angular offset  $\beta$  (e.g.,  $0^{\circ} < \beta < 90^{\circ}$  or  $90^{\circ} < \beta < 180^{\circ}$ ) relative to the first.
- (b) Parallel layout: The two turbines are positioned laterally, perpendicular to the inflow ( $\beta = 90^{\circ}$ ).
- (c) Tandem layout: The second turbine is aligned directly down-stream of the first ( $\beta=0^{\circ}$ ).

Currently, research on interacting VAWT pairs focuses primarily on the aerodynamic performance under these three relative arrangements.

### 1.1.1. Inflow angle

Schatzle et al. [28] were the first to investigate the influence of inflow angle on the performance of two Darrieus-type VAWTs. They examined the aerodynamic interference between two VAWTs with a fixed turbine spacing of 1.5 rotor diameters under eight discrete relative orientations. Their results showed that a significant reduction in the power of the downstream turbine occurred only when the two turbines were arranged in a tandem configuration with respect to the incoming wind direction, while other orientations exhibited performance nearly identical to that of an isolated turbine. Further analysis revealed that this power loss increased with tip speed ratio (TSR) and was primarily caused by wake-induced changes in flow angularity, rather than by a significant reduction in total flow velocity.

Rajagopalan et al. [29] studied the impact of inflow angle on the power coefficient of two straight-bladed Darrieus-type VAWTs. Their findings indicated that at larger  $\beta$  values, both turbines exhibited higher average power coefficients compared to an isolated unit. Moreover, studies on counter-rotating straight-bladed Darrieus VAWTs [30] and co-rotating Savonius-type VAWTs [31] both demonstrated that a parallel layout outperforms staggered configurations with small  $\beta$  values in terms of aerodynamic performance. Additionally, Sahebzadeh et al. [32] reported that for co-rotating straight-bladed Darrieus VAWTs, the optimal  $\beta$  angle was approximately 75°.

It is evident that the tandem arrangement of two VAWTs is the least favorable configuration, as the downstream turbine suffers severe aerodynamic degradation due to the wake of the upstream one. Therefore, such a layout should be avoided in wind farm design.

# 1.1.2. Rotation direction

As early as 2004, Thomas [33] emphasized the critical role of rotation direction in wind farm layout optimization. When two adjacent

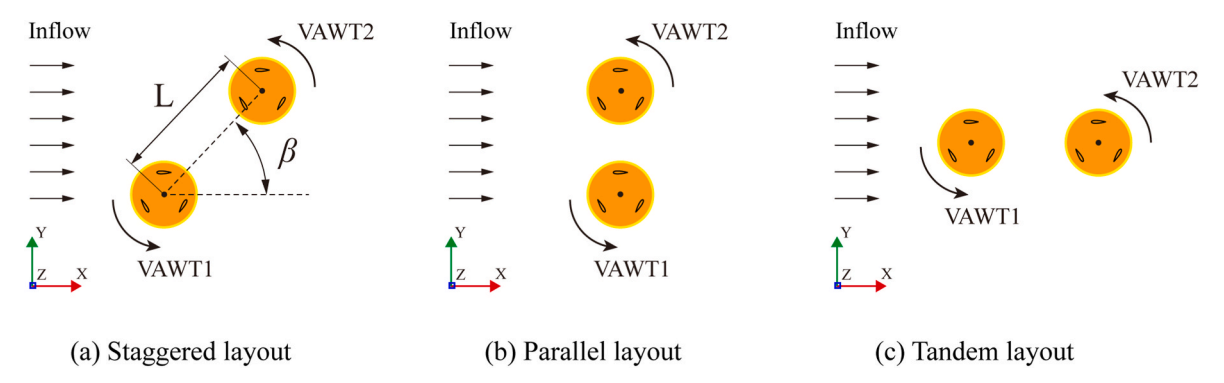


Fig. 1. Three typical layouts of two VAWTs with respect to the incoming wind direction.

VAWTs rotate counter-rotating downstream, their wake interactions can enhance the overall aerodynamic performance. For two Darrieus-type VAWTs arranged in a parallel layout, studies have shown that counter-rotating downstream configurations outperform counter-rotating upstream setups in terms of efficiency [34,35]. Additionally, other research indicates that co-rotating arrangements exhibit higher efficiency than counter-rotating upstream configurations [36].

Sun et al. [37] observed similar trends in their study of two Savonius-type hydro turbines in a parallel layout. Jang et al. [38] further reported that, for two Savonius-type VAWTs, co-rotation produced a higher power coefficient than counter-rotation. This result was attributed to the low wind speed conditions under which the experiments were conducted. Supporting this, Ahmadi-Baloutaki et al. [39] found that co-rotating configurations perform better under low wind speeds, whereas counter-rotating downstream configurations become more advantageous at high wind speeds.

For staggered layouts, the study by Shaheen and Abdallah [40] showed that, in co-rotating configurations, placing VAWT2 downstream of VAWT1 is more effective than placing it upstream. However, in both cases, the counter-rotating downstream configuration consistently yielded the highest efficiency. This phenomenon is mainly attributed to the alignment of induced flow between the two VAWTs with the free-stream direction, reducing vertical shear, lowers turbulence and energy dissipation, and ultimately enhancing power output [41].

Zheng et al. [42] emphasized that in parallel layouts, power augmentation is primarily due to the confinement of lateral airflow between turbines. In contrast, in staggered layouts, the presence of the upstream turbine accelerates the surrounding flow, contributing to the improved performance of the downstream unit. In tandem layouts with large inter-turbine spacing, counter-rotating configurations are more effective than co-rotating ones in enhancing the downstream VAWT's power coefficient, as counter-rotation induces wake deflection from the upstream turbine, thereby improving the aerodynamic environment for the downstream unit [43].

Therefore, rotational direction directly influences the wake deflection behavior of VAWTs. In staggered layouts, positioning the downstream turbine outside the wake of the upstream VAWT is essential for improving aerodynamic performance.

### 1.1.3. Turbine spacing

When two VAWTs are placed too closely together, the airflow between them becomes obstructed, hindering effective flow passage through the inter-turbine gap. In such cases, the two turbines behave aerodynamically like a blunt body, increasing the overall drag coefficient and leading to reduced power output [44].

For co-rotating H-type VAWTs in a staggered layout, the optimal spacing tends to decrease with increasing  $\beta$  [45]. In tandem layouts, increasing the distance between turbines improves the average power coefficient. However, in parallel layouts, greater turbine spacing may reduce the beneficial aerodynamic interaction, and the optimal spacing is generally less than 1.25 times the rotor diameter (D) [46]. Similar findings were reported by Giorgetti et al. [47] and Tavernier et al. [48].

Bangga et al. [49] found that for H-type VAWTs in a parallel layout, the optimal spacing is 2D for counter-rotating downstream configurations. For co-rotating configurations, the optimal spacing increases further, while for counter-rotating upstream configurations, the optimal spacing exceeds 4D. This indicates that counter-rotating upstream arrangements are least favorable for wind farm performance due to their blockage effect on the flow, whereas counter-rotating downstream layouts allow for closer turbine spacing. Therefore, the optimal VAWT spacing is not only influenced by the inflow angle but also by the rotation direction and other layout parameters.

### 1.2. Research motivation and novelties

In summary, practical wind farm design should comprehensively

consider multiple factors, including turbine spacing, inflow angle, and rotation direction, to achieve optimal power output. Despite promising advancements in VAWT technology, several fundamental questions remain unresolved and hinder the scalability of VAWT arrays, particularly in offshore applications. This study is motivated by three key knowledge gaps:

- (1) Most existing studies on VAWT array layouts have focused on small-scale, bottom-fixed configurations with sub-meter blade lengths, typically operating at Reynolds numbers in the range of 10<sup>5</sup> - 10<sup>6</sup>. These investigations often report enhanced power output under closely spaced conditions. However, the aerodynamic benefit of large-scale VAWTs operating at higher Reynolds numbers (~10<sup>7</sup>) have not been well studied.
- (2) Although floating VAWTs are increasingly recognized for their potential in deep-sea offshore deployment, no prior research has addressed the layout optimization of floating VAWT arrays. Consequently, there remains a limited understanding of how these systems perform at the wind farm scale under realistic environmental loads. By contrast, studies on HAWT arrays are relatively mature: fixed-bottom cases have examined yaw-based control [50,51] and wake interactions between adjacent turbines [52,53], while floating HAWTs have been analyzed in terms of platform motion effects on aerodynamics and wakes [54,55]. Compared with fixed-bottom VAWTs, floating counterparts are subject to six-degree-of-freedom (6-DOF) motions that can modify inflow, deflect wakes, and amplify unsteady loading, thereby making array optimization inherently more challenging and necessitating a fully coupled aero—hydro—mooring approach.
- (3) Floating VAWTs are subject to strong coupling between aerodynamic forces, wave-induced platform motion, and mooring dynamics. While the blade-level aerodynamic effects of platform motions for the same turbine design have been investigated in our previous work [58], the influence of six-degree-of-freedom platform response on the performance of VAWT arrays, especially under staggered configurations, remains insufficiently understood and is the focus of the present study.

To address these knowledge gaps, this study develops a fully coupled aero—hydro—mooring simulation framework to analyze staggered floating VAWT arrays. By clarifying the physical mechanisms underlying array-scale interactions and quantifying the associated performance benefits, the findings aim to reduce the perceived risks of floating VAWT deployment and support their scalable implementation in offshore wind energy projects.

The outline of the paper is organized as follows: Section 2 presents the numerical framework and modeling approach. Section 3 introduces the system configuration, solver settings, and mesh strategies. Section 4 provides a comprehensive analysis of wind farm performance under various array layouts and examines the coupled aero-hydrodynamic responses of staggered floating VAWTs.

# 2. Methodology

# 2.1. DFBI module

In STAR-CCM+, the coupling between the fluid and the six-degree-of-freedom (6-DOF) rigid body is referred to as dynamic fluid body interaction (DFBI). Under unconstrained conditions, the rigid body can move freely in all directions, and its dynamic behavior is simulated by solving the translational and rotational motion equations of the center of mass. Based on the global coordinate system, the translational motion of the rigid body is governed by:

$$md\mathbf{v} / dt = \mathbf{f} \tag{1}$$

where m denotes the mass of the rigid body, f is the total external force acting on the rigid body, and v is the velocity of its center of mass.

The rotational motion of the rigid body is expressed in the local coordinate system fixed at the center of mass as:

$$\mathbf{M}d\omega / dt + \omega \times \mathbf{M}\omega = \mathbf{n} \tag{2}$$

$$\mathbf{M} = \begin{pmatrix} M_{xx} & M_{xy} & M_{xz} \\ M_{xy} & M_{yy} & M_{yz} \\ M_{xz} & M_{yz} & M_{zz} \end{pmatrix}$$
(3)

where  $\omega$  is the angular velocity vector,  $\mathbf{n}$  is the total external moment acting on the rigid body, and  $\mathbf{M}$  is the moment of inertia tensor. Due to its symmetry, the inertia tensor can be defined using its diagonal terms  $(M_{xx}, M_{yy}, M_{zz})$  and off-diagonal terms  $(M_{xy}, M_{xz}, M_{yz})$ .

The DFBI approach enables the simulation of rigid body motion induced by external fluid forces. When combined with the built-in solid stress solver in STAR-CCM+, DFBI can also be used to model deformable or partially deformable bodies, thereby enabling fluid–structure interaction (FSI) simulations. The overall modelling framework of the DFBI method is illustrated in Fig. 2.

As shown in Fig. 2, the DFBI module is used to solve the 6-DOF motion of the entire floating system, while the solid stress solver can be employed to calculate local or global deformations of the floating VAWT. On the fluid side, the finite volume method (FVM) combined with the turbulence model is adopted to capture viscous effects, wave diffraction, radiation, impact, and run-up phenomena, thereby enabling accurate computation of hydrodynamic loads acting on the floating platform. The Volume of Fluid (VOF) multiphase model is used to track the air—water interface and simulate the fluid distribution and dynamic behavior under the influence of floating structures.

In this study, the floating VAWT is modeled as a rigid body with 6-DOF using the DFBI method. Blade deformation is not considered during the simulation process. It is worth noting the following considerations: i. The mooring system in the DFBI module is modeled using a quasi-static catenary approach, which neglects the dynamic contact between the mooring lines and the seabed; ii. The solid stress solver lacks a comprehensive material database, thus the composite properties of wind turbine blades are not considered; iii. Key parameters of the

floating system, such as the center of gravity, moments of inertia, and other mass-related properties, are predefined in the software, and the structural characteristics of the actual wind turbine are not explicitly modeled.

Since the entire coupling process is integrated within STAR-CCM+, data exchange with third-party CAE solvers is avoided, which significantly improves computational efficiency. Therefore, the DFBI-coupled model is suitable for the preliminary design and rapid evaluation of the aero-hydrodynamic performance of floating VAWTs. For more complex structural dynamic analyses, coupling with external CAE solvers is required.

### 2.2. VOF wave model

To capture the evolution of the free surface between air and water, the VOF model is adopted within the STAR-CCM+. This interface-capturing method enables the accurate resolution of immiscible phase boundaries by solving transport equations for the phase volume fraction fields. It assumes that the mesh resolution is sufficiently refined to resolve the interface topology across cells.

The volume fraction of phase i in each computational cell is defined as:

$$a_i = \frac{V_i}{V} \tag{4}$$

where  $V_i$  is the volume occupied by phase i, and V is the total volume of the cell. The sum of volume fractions over all N phases satisfy the following constraint:

$$\sum_{i=1}^{N} a_i = 1 \tag{5}$$

In this study, water is defined as the primary phase in the VOF framework, and its volume fraction is directly solved via the transport equation. The volume fraction of air is obtained by enforcing the constraint  $a_{air}+a_{water}=1$ , without solving an additional equation. Surface waves are generated using a fifth-order approximation to Stokes wave theory, as implemented in the VOF-based wave model of STAR-CCM+. This approach more accurately represents real ocean waves than lower-order

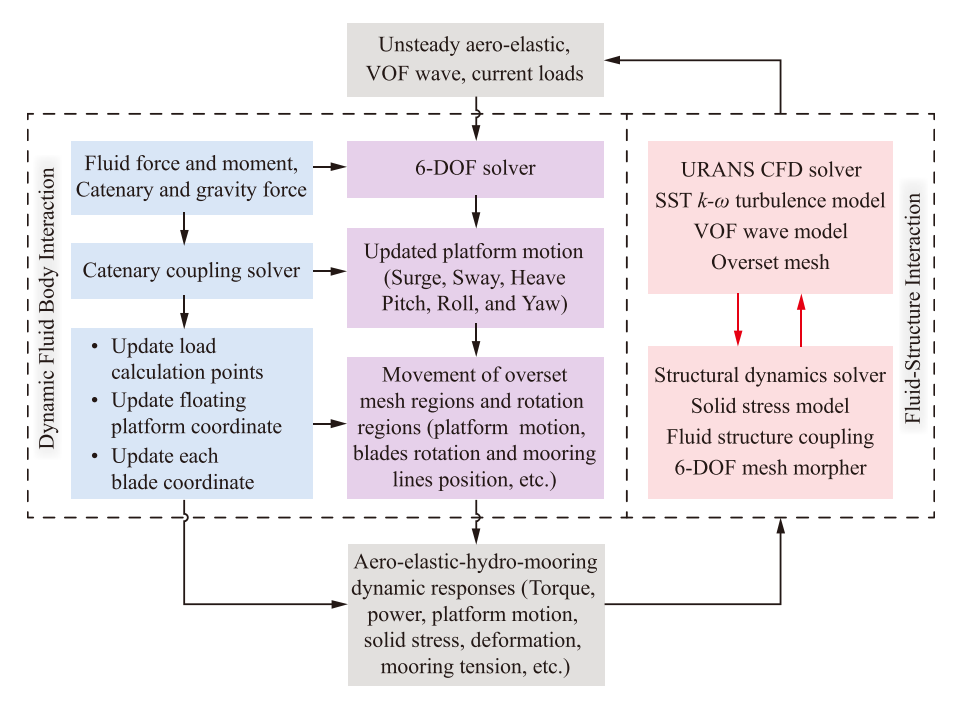


Fig. 2. Fully coupled framework.

methods, particularly in intermediate to deep water depths where nonlinear effects become significant. The wave profile and phase velocity are functions of the wave height, wavelength, and local water depth.

The nonlinearity of the wave motion is characterized by the Ursell number [56], defined as:

$$U_{R} = \frac{H\lambda^{2}}{d^{3}} \tag{6}$$

where H is the wave height,  $\lambda$  is the wavelength, and d is the water depth. The fifth-order Stokes wave model is valid for Ursell numbers less than 30.

To prevent wave reflection from domain boundaries, a wave damping zone is applied near the outlet. The damping is achieved by introducing a vertical resistance term to the  $\omega$ -velocity equation, following the method proposed by Choi and Yoon [57]. The added source term  $S_z^d$  in the momentum equation is expressed as:

$$S_z^d = \rho(f_1 + f_2|\omega|) \frac{e^x - 1}{e^1 - 1} \omega \tag{7}$$

$$\kappa = \left(\frac{x - x_{sd}}{x_{ed} - x_{xd}}\right)^{n_d} \tag{8}$$

where  $\omega$  is the vertical velocity component,  $\rho$  is the fluid density, and  $f_1$ ,  $f_2$  and  $n_d$  are the damping coefficients.  $x_{sd}$  and  $x_{ed}$  are the start and end positions of the damping region along the wave propagation direction.

The effectiveness of the damping zone is quantified by the damping strength ratio  $r^d$ , given by:

$$r^d = \frac{e^x - 1}{e^1 - 1} \tag{9}$$

Eq. (9) ensures gradual energy absorption and minimizes spurious wave reflection from the outlet boundary, enabling stable and realistic wave–structure interaction simulations.

### 2.3. Mooring model

In this work, the mooring system is modeled using an elastic, quasistatic catenary formulation embedded in the DFBI framework of STAR-CCM+. This approach captures the equilibrium profile of a flexible mooring line suspended between two end points  $(p_1 \text{ and } p_2)$  under the influence of its own weight and axial tension (see Fig. 3), and is particularly suitable for floating wind turbine simulations under moderate platform excursions.

The spatial shape of the mooring line is determined in a local cartesian coordinate system via a set of parametric equations.

The curve shape of the catenary in a state of force equilibrium is defined as follows:

$$x(u) = au + b \sinh(u) + \alpha \tag{10}$$

$$y(u) = a\cosh(u) + \frac{b}{2}\sinh^2(u) + \beta \tag{11}$$

$$u_1 \le u \le u_2 \tag{12}$$

where  $\alpha$  and  $\beta$  are integration constants reflecting the global position of the line, and u is a non-dimensional curve parameter. The coefficients a, b, and c incorporate the physical properties of the line:

$$a = \frac{c}{\lambda_0 g}, b = \frac{ca}{DL_{eq}}, c = \frac{\lambda_0 L_{eq} g}{\sinh(u_2) - \sinh(u_1)}$$
(13)

where  $\lambda_0$  is the line mass per unit length,  $L_{eq}$  is the relaxed (unstretched) length of the mooring line, D is the axial stiffness of the line, and g is the gravitational acceleration.

The inclination angle  $\phi$  of the mooring curve at a given parameter value  $\boldsymbol{u}$  is related by:

$$tan \phi = \sinh(u) \tag{14}$$

The end-point forces  $\mathbf{f}_1$  and  $\mathbf{f}_2$ , acting on the floating platform from each mooring line, are obtained from the local tangent direction of the catenary profile at  $u=u_1$  and  $u=u_2$ , respectively:

$$\mathbf{f}_{1} = \begin{bmatrix} f_{1,x} \\ f_{1,y} \end{bmatrix} = \begin{bmatrix} c \\ c \sinh(u_{1}) \end{bmatrix}, \mathbf{f}_{2} = \begin{bmatrix} -c \\ -c \sinh(u_{2}) \end{bmatrix}$$
(15)

These forces are resolved in the global coordinate system and incorporated into the external load vector driving the 6-DOF motion of the floating wind turbine platform.

It should be noted that this quasi-static model does not consider dynamic seabed contact or line-soil interaction. However, by eliminating the need for full dynamic resolution or third-party coupling, it provides a computationally efficient approximation of mooring-induced restoring forces. This makes it particularly suitable for early-stage design and aero-hydrodynamic performance evaluation of floating wind turbines.

### 3. Numerical model and solver setting

# 3.1. Staggered floating VAWTs

The floating VAWT system investigated in this study consists of two identical and independently floating VAWTs, each mounted on its own platform, as shown in Fig. 4. The turbines are arranged in a staggered configuration and are subjected to combined wind and wave loads. Each turbine features an H-type design originally proposed by Liu et al. [58], with three straight blades spaced 120° apart around a central shaft and supported by two horizontal arms positioned at the top and bottom.

The main geometric and operational parameters of the VAWT are

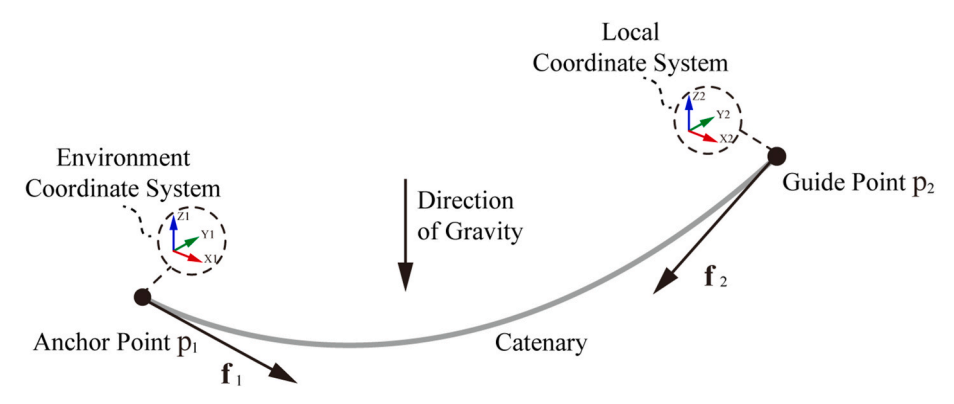


Fig. 3. Catenary forces in the DFBI framework.

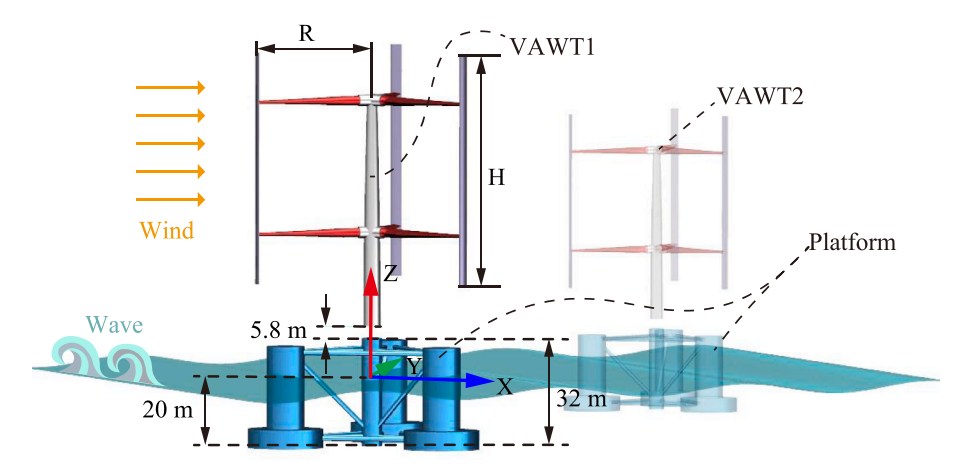


Fig. 4. Geometric model of the floating VAWT.

summarized in Table 1. The rotor has a radius (R) of 36.76 m and a height (H) of 70.25 m, with a vertical distance of 5.8 m between the platform and the tower connection point - originally designed to accommodate the nacelle and drivetrain. Detailed modeling procedures and the spatial geometry of the support rods and tower structure can be found in Refs. [58,59]. The environmental conditions consist of aligned wind and regular waves propagating in the same direction.

The floating VAWT in this study is supported by a semi-submersible platform adapted from the NREL OC4 reference design [60], as illustrated in Fig. 5. The platform consists of cylindrical columns, including upper and lower pontoons and a central main column, which are structurally connected by cross and diagonal braces. This configuration provides both hydrodynamic stability and sufficient buoyancy under combined wind and wave loads.

To ensure proper draft and restoring moments, ballast water is internally allocated within the upper and lower pontoons, with heights of 7.83 m and 5.17 m, respectively. The VAWT tower is mounted on the central main column, meaning that the platform is directly subjected to gravitational loads and gyroscopic moments induced by VAWT operation. It is worth noting that, for the convenience of numerical modeling, the connection points between the diagonal braces and the pontoons have been slightly adjusted. The red diagonal brace shown in Fig. 5a indicates the original design position in the OC4 configuration.

The mass-related properties of the floating platform, obtained by assigning material properties in the third-part CAE software ABAQUS, are summarized in Table 2. As shown, the computed results exhibit excellent agreement with the reference values reported in the OC4 documentation [60]. Minor discrepancies are observed in the moment of inertia along the pitch, roll, and yaw directions. These deviations remain within an acceptable range and are likely attributed to the slight adjustments made to the diagonal brace geometry in the current study for modeling purposes.

The floating VAWT is stabilized by three mooring lines connected to the platform, as shown in Fig. 6. Mooring line M2 is aligned with the

**Table 1**Geometric parameters of the floating VAWT.

Parameter/Unit	Value		
Blade Airfoil	DU-06-W-200		
Number of Blades	3		
Number of Support Rods per Blade	2		
Blade Height H/m	70.25		
Rotor Radius R/m	36.76		
Blade Chord Length c/m	3.512		
Blade Pitch Angle $\beta/^{\circ}$	2		
Optimal TSR λ/N	3.28		
Rated Rotational Speed $\omega$ /rpm	6.81		

wind and wave direction, while M1 and M3 are symmetrically arranged  $120^{\circ}$  apart around the platform in a radial configuration. Each mooring line is anchored to the upper section of the lower pontoon at one end, and to a fixed seabed anchor point at the other. Due to the influence of gravity, the mooring line naturally forms two distinct segments: a free-hanging (suspended) segment and a seabed-contact (laid-down) segment, as shown in Fig. 6b.

In this study, the quasi-static catenary modeling approach introduced in Section 2.3 is employed to calculate mooring line tension. This method determines the shape and tension distribution of the mooring lines by solving the static equilibrium equations.

As a result, seabed contact effects are not included, and the seafloor is neglected during the simulation. The mooring lines are thus treated as flexible cables suspended between the platform and the surrounding marine environment, with their shape influenced solely by self-weight and boundary tension, as shown in Fig. 7.

The main mass-related properties of the mooring line are summarized in Table 3. According to the OC4 report [60], two values are available for the equivalent mass density: the dry mass density (113.35 kg/m) and the submerged mass density (108.63 kg/m). In this study, the latter is adopted, as it more accurately represents the effective weight of the mooring line in water, considering the buoyancy effect.

# 3.2. Numerical settings and verification

To simulate the staggered floating VAWT configurations described in Section 3.1, a computational domain containing both air and water phases is established, as shown in Fig. 8. The domain size is set to 1200 m (length)  $\times$  650 m (width)  $\times$  500 m (height), in the streamwise (X), spanwise (Y), and vertical (Z) directions. To suppress wave reflection and resonance, a wave damping zone is applied in the downstream region, starting 300 m upstream of the pressure outlet.

At the velocity inlet, both wind and wave propagate in the positive X direction. Regular waves are generated using the VOF-based wave model described in Section 2.2, with the corresponding parameters listed in Table 4. These wave conditions are representative of those frequently observed in high-sea states in the North Atlantic, based on ocean data retrieved from Buoyweather [61] at latitude  $60.8^{\circ}$  N and longitude  $27.8^{\circ}$  W. This location is known for exhibiting some of the most extreme sea states encountered globally.

Fig. 9 illustrates the mesh distribution for the staggered floating VAWT configuration, which was generated using the Trimmed Cell Mesher in STAR-CCM+ 16.08. A total of 24.23 million orthogonal, isotropic, and structured volume cells were employed. Near-wall regions were refined using prism layer meshes to accurately capture boundary layer behavior, which is essential for turbulence modeling. The shear stress transport (SST)  $k-\omega$  turbulence model was employed to resolve

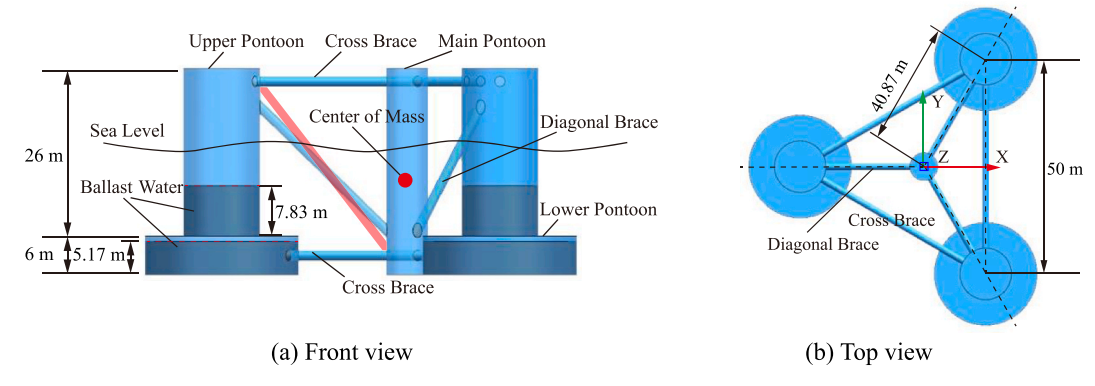


Fig. 5. Geometry model of semi-submersible platform.

**Table 2**Comparison of mass-related properties of the floating platform with OC4 report [60].

Structural Parameter/Unit	Value in Ref [9]	Value in FEM value	Error
Mass (including ballast water)/	$1.3473\times10^7$	$1.3473\times10^7$	0.0 %
Center of Mass (below waterline)/m	13.46	13.46	0.0 %
Roll Moment of Inertia Ixx/kg·m <sup>2</sup>	$6.827 \times 10^{9}$	$6.56 \times 10^{9}$	-3.9 %
Pitch Moment of Inertia  I <sub>yy</sub> /kg·m <sup>2</sup>	$6.827\times10^9$	$6.56\times10^9$	-3.9 %
Yaw Moment of Inertia $I_{zz}/kg \cdot m^2$	$1.226\times10^{10}$	$1.17\times10^{10}$	-4.6 %

the near-wall and separated flows around the VAWTs. This model has been widely adopted in offshore wind turbine simulations for its balance between robustness and accuracy in capturing adverse pressure gradients. The validation of this turbulence model for floating VAWT applications can be found in the authors' previous work [58,59].

The overset mesh technique was applied to handle the rotor rotation and the platform's 6-DOF motion relative to the background mesh. The hydrodynamic response of the floating platform was preliminarily verified through free-decay tests, which were conducted and discussed

in detail in the authors' previous work [58,59].

To accurately resolve wake interactions and vortex shedding, local mesh refinement was implemented in the wake region of rotors and trailing edge of VAWT blades. On the blade surfaces, trimmed meshes were generated using the STAR-CCM + Trim Mesh model, with an orthogonal and isotropic distribution that ensures consistent in-surface cell size along both chordwise and spanwise directions. Mesh independence verification is presented in Table 5, where three mesh schemes with varying overset region and blade surface resolutions were compared. The results show that further mesh refinement beyond the medium resolution leads to minimal changes in power coefficient. Although the cell sizes of overset region and blade surface were halved from the medium to the fine mesh, the variation in power coefficients for

**Table 3**Mass-related parameters of mooring system.

Structural Parameter/Unit	Value	
Relaxation length $l_c/m$	835.5	
Cross-sectional diameter $d_c/m$	0.0766	
Mass density/kg/m	113.35	
Mass density in water/kg/m	108.63	
Stiffness/N/m	$7.536 \times 10^{8}$	

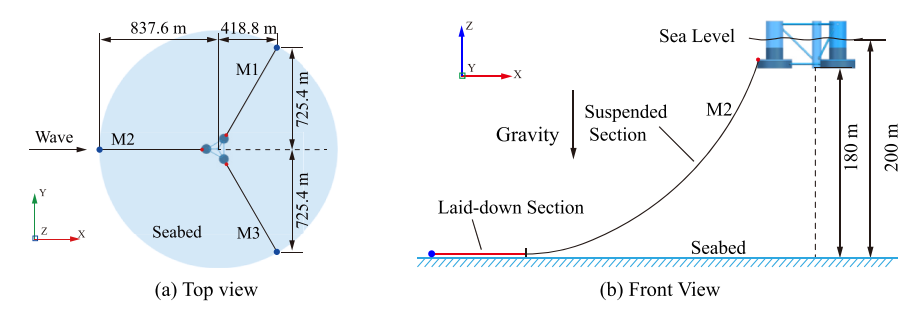


Fig. 6. Layout and anchoring configuration of mooring lines for the floating platform.

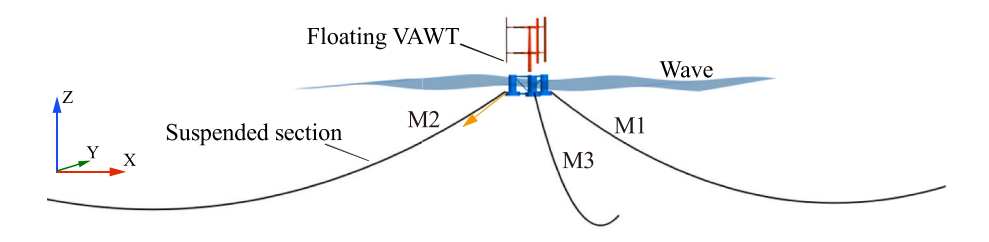
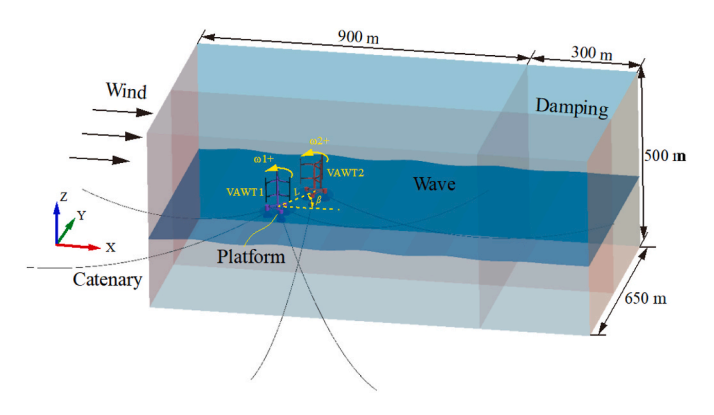


Fig. 7. Catenary configuration of mooring lines in the DFBI simulation.



 $\begin{tabular}{ll} \textbf{Fig. 8.} Computational domain and boundary conditions for staggered floating VAWTs. \end{tabular}$ 

**Table 4**Input parameters for wave generation using VOF model.

Structural Parameter/Unit	Value	
Wave height/m	7.58	
Wave depth/m	200	
Wave period/s	12.1	
Wave length/m	231.02	
Water density/kg/m <sup>3</sup>	1025	
Dynamic viscosity/Pa•s	$8.9 \times 10^{-4}$	

both VAWT1 and VAWT2 remained below 0.4 %. In addition, for wave modeling, the grid spacing was set to  $\Delta x = \Delta y = 2.5$  m in the horizontal plane and  $\Delta z = 0.625$  m in the vertical direction. This configuration satisfies the widely adopted requirement of at least 12 cells per wave

height [62,63] and provides a resolution finer than the 1/80 wavelength criterion along the wave direction [64]. Thus, it ensures sufficient accuracy in capturing the free-surface evolution and wave kinematics while keeping the computational cost tractable. Therefore, the medium-resolution mesh was selected for subsequent simulations to balance numerical accuracy and computational cost.

In addition, special attention was given to the near-wall treatment. An 8-layer prism boundary layer mesh was applied around all solid surfaces, with the first-layer thickness set to 0.0075 m and a total thickness of 0.3 m. Given the full-scale nature of the modeled floating VAWTs, a fully wall-resolved mesh with  $y+\approx 1$  across all blade surfaces would result in an extremely large number of cells. Instead, the wall-function approach was adopted, which is widely used in large-scale wind turbine simulations. As shown in Fig. 10, most blade surface cells fall within  $50 \le y+ \le 150$ , ensuring consistency with the recommended range for wall-function-based SST  $k-\omega$  turbulence modeling.

A segregated flow solver was used to sequentially solve the integral conservation equations for mass and momentum. A pressure–velocity coupling was handled using the SIMPLE algorithm, which follows a

**Table 5**Grid independence verification for staggered floating VAWTs.

Parameters Coarse mesh		Medium mesh	Fine mesh	
Rotor wake size [m]	2.5 m	1.25 m	1.25 m	
Overset region size [m]	2.5 m	1.25 m	0.625 m	
Blade surface size [m]	0.3 m	0.15 m	0.075 m	
Blade wake size [m]	0.625	0.3125 m	0.3125 m	
Total cell count	18241745	24238345	29586879	
$C_{\rm p}$ of VAWT1 $C_{\rm p}$ of VAWT2	0.3037 0.3152	0.3130 0.3234	0.3138 0.3246	

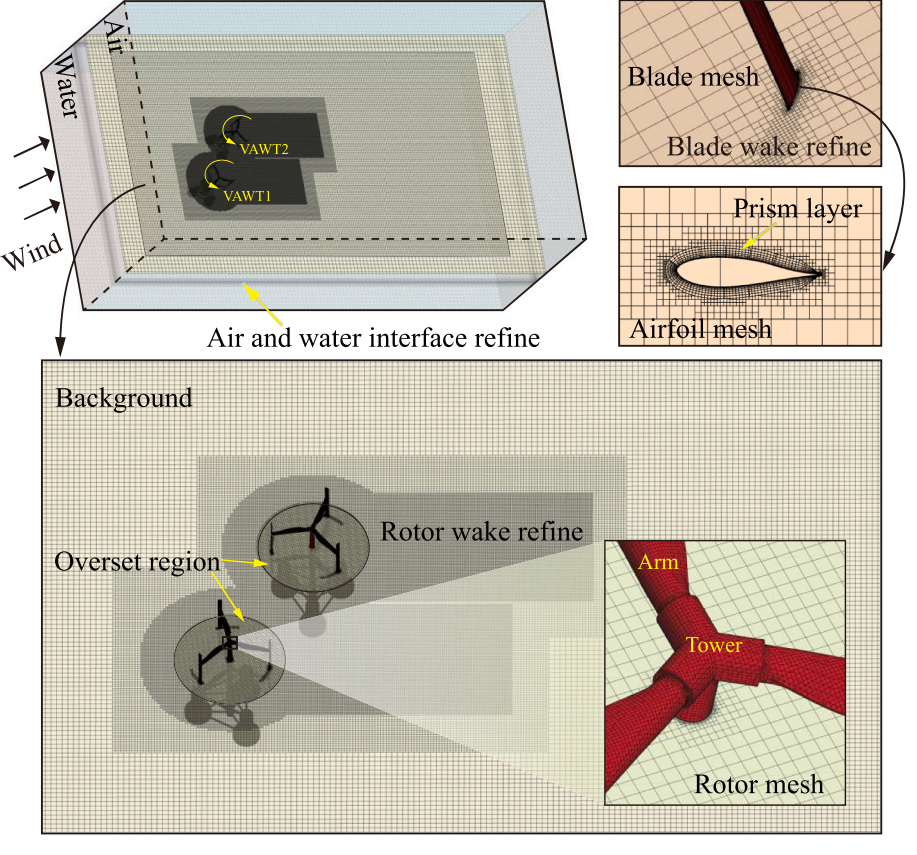
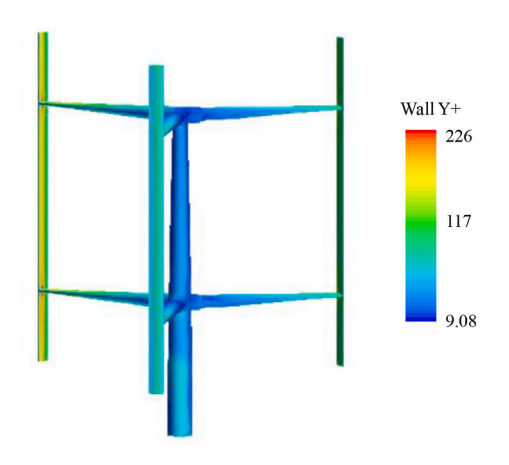


Fig. 9. Mesh distribution and local refinement strategy for staggered floating VAWTs.



**Fig. 10.** The wall y + distribution of the floating VAWT rotor.

predictor–corrector strategy where a pressure correction equation is iteratively solved to enforce mass conservation. In the simulation process, an initial solution was obtained using a first-order upwind scheme, which was then switched to a second-order upwind scheme to improve convective accuracy and reduce numerical diffusion.

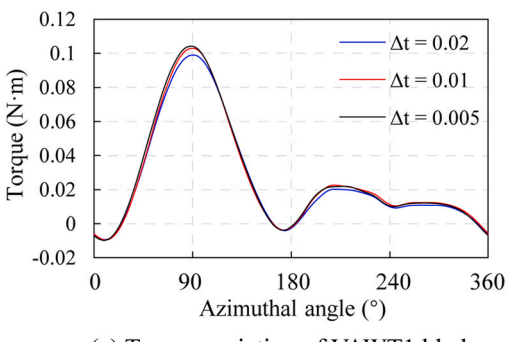
Time-step independence test was conducted using three different time steps (0.005s, 0.01s, and 0.02 s), and the corresponding torque results are shown in Fig. 11.

In Fig. 11, the torque responses of VAWT1 and VAWT2 exhibit clear convergence trends as the time step decreases. For VAWT1 (Fig. 11a), the torque profiles remain largely consistent across different time steps, with only minor differences in peak values near the azimuthal angle of  $90^{\circ}$ . In contrast, VAWT2 (Fig. 11b) shows a more pronounced sensitivity to time step refinement, particularly in the region of  $60^{\circ}$ –120°, where the torque peak noticeably increases as the time step is reduced. This indicates that the downstream turbine (VAWT2) experiences more unsteady wake-induced fluctuations, requiring finer temporal resolution to accurately capture the dynamic loads. Overall, the results confirm that a time step of 0.01 s achieves sufficient temporal accuracy for both turbines and is thus used in the subsequent simulations.

## 4. Results and discussion

In this section, an orthogonal experimental design (OED) approach is first employed to systematically assess the effects of different staggered layout configurations on the aerodynamic performance of bottom-fixed VAWTs. Based on these findings, the feasibility of applying staggered layouts to floating VAWTs is subsequently investigated.

All simulations were conducted on the Prospero high-performance computing (HPC) cluster at Liverpool John Moores University. For the baseline case involving a single isolated VAWT, 2 compute nodes with 64 cores each (total 128 cores) were employed. Each simulation



(a) Torque variation of VAWT1 blade

required approximately 72–80 h to complete 25 rotor revolutions, corresponding to about 220 s of physical time. For bottom-fixed VAWT configurations, including staggered, parallel, and tandem layouts, 4 nodes (256 cores) were used to accommodate the increased computational demand associated with simulating two interacting turbines. The simulation duration remained similar, requiring approximately 72–80 h. In contrast, the floating VAWT case with a staggered layout required significantly more computational resources due to the 6-DOF platform motion modeled via DFBI and the increased mesh density in the VOF region. This setup was run on 6 nodes (384 cores), simulating 40 rotor revolutions (approximately 360 s of physical time), with a total wall-clock time of about 144–150 h per case.

### 4.1. Optimization of staggered layout parameters

An optimization of staggered layout parameters is conducted for two bottom-fixed VAWTs with identical geometric configurations. The computational domain and boundary conditions are shown in Fig. 12. Both VAWT1 and VAWT2 operate at the same rotational speed of 6.81 rpm, corresponding to the optimal TSR of 3.28. Additionally, by rotating the blades by  $180^{\circ}$ , both co-rotating and counter-rotating configurations can be implemented without modifying the geometry of the supporting arms and tower structures.

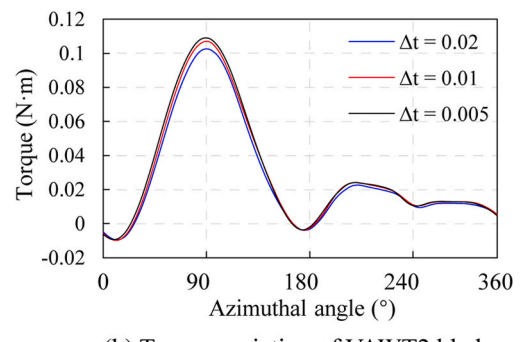
### 4.1.1. Orthogonal experimental design

The layout parameters considered include the turbine spacing (Factor A), the inflow angle (Factor B) between the wind direction and the centerline connecting the two-turbine rotation center, and the rotation direction (Factor C). Each factor is set three levels, as listed in Table 6.

The turbine spacing is initially set to 1.5D and increased in increments of 0.5D. Based on previous studies on small-scale VAWTs [20], an optimal inflow angle of approximately  $60^{\circ}$  has been reported; Therefore, three angles  $(45^{\circ}, 60^{\circ}, \text{ and } 75^{\circ})$  are selected for evaluation. The rotation direction includes co-rotating (both VAWTs rotate in the same direction), counter down (VAWT1 rotates counterclockwise, VAWT2 clockwise), and counter up (VAWT1 clockwise, VAWT2 counterclockwise).

In this study, the co-rotating case was defined as both turbines rotating counterclockwise. Under the uniform inflow conditions, a clockwise co-rotating case is equivalent to a mirrored configuration with a negative inflow angle. This mirror symmetry ensures that the array-scale scalar indicators remain unchanged, even though the lateral deflection direction of the wakes differs. To maintain a compact orthogonal design, only the counterclockwise co-rotating case was included. The asymmetric counter-rotating cases (Counter down and Counter up) were introduced specifically to capture the effects of relative rotation direction on wake deflection.

By combining the three factors at three levels, a total of nine staggered layout cases are designed based on the  $L_9$  (3<sup>4</sup>) orthogonal array as shown in Fig. 13.



(b) Torque variation of VAWT2 blade

Fig. 11. Time step sensitivity analysis for staggered floating VAWTs.

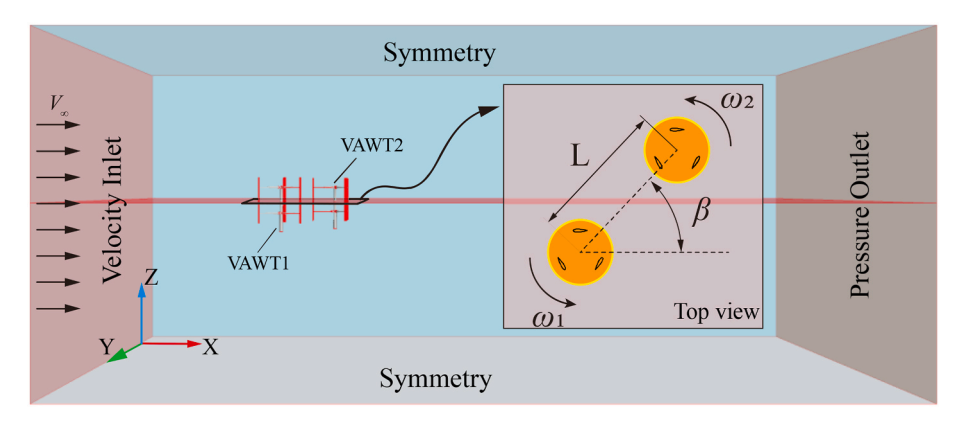


Fig. 12. Computational domain and boundary conditions for staggered bottom-fixed VAWTs.

**Table 6**Design factors and levels of staggered bottom-fixed VAWTs.

Factor	or Spacing/A Inflow angle/B		Rotation direction/C	
Level 1	1.5D	45°	Co-rotating	
Level 2	2D	60°	Counter down	
Level 3	2.5D	75°	Counter up	

To evaluate the effectiveness of different staggered layout configurations of VAWTs, the performance indicator  $(\Omega)$  is introduced. This dimensionless metric quantifies the relative performance gain achieved by multiple turbines operating simultaneously in a layout, compared to

their standalone operation. It is defined as follows [20]:

$$\Omega = \frac{\sum_{i=1}^{n} C_{P_i}}{n \cdot C_{P_{box}}} \tag{16}$$

where:  $C_{P_i}$  is the power coefficient of the *i*-th VAWT within the staggered layout,  $C_{P_{loo}}$  is the power coefficient of a single VAWT operating in isolation, and n is the total number of VAWTs in the layout. Therefore, if  $\Omega > 1$ , the staggered layout achieves a total power output that exceeds the sum of the outputs of n VAWTs operating independently.

To further quantify the contribution of each individual turbine to the total performance, a normalized indicator  $\Omega_i$  is introduced as:

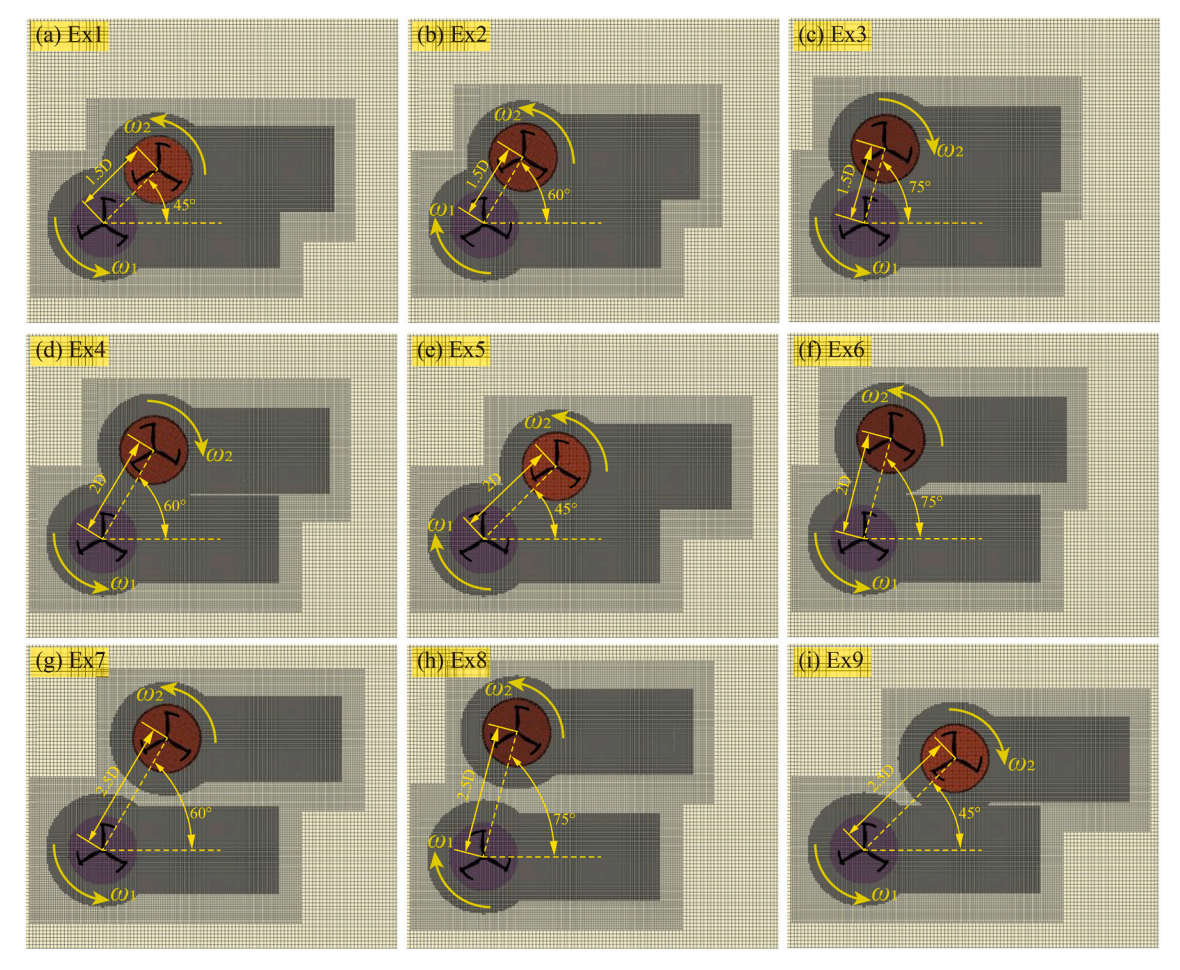


Fig. 13. Mesh distribution of bottom-fixed VAWTs in different staggered layout.

$$\Omega_i = \frac{C_{P_i}}{C_{P_{i-}}} \tag{17}$$

Eq. (17) enables an intuitive comparison of each turbine's performance relative to its isolated baseline.

### 4.1.2. Range analysis

A range analysis is conducted on the OED results, which allows rapid identification of the factors that have a significant impact on wind farm performance.

The value of the performance indicator  $\Omega$  corresponding to the nine OED schemes are summarized in Table 7. In the table,  $K_i$  (where i=1,2,3) denotes the average value of  $\Omega$  for all cases at level i of a given factor. The range  $R(\mu)$  represents the difference between the maximum and minimum  $K_i$  values for each factor  $\mu$  (where  $\mu=A$ , B, C corresponds to spacing, inflow angle, and rotation mode, respectively).

As shown in Table 7, factor B exhibits the largest range  $R(\mu)$ , indicating that the inflow angle  $\beta$  has the most significant influence on the performance of the staggered layout. The influence of the three factors on the wind farm performance decreases in the order of R(B) > R(A) > R(C). The relationship between each factor level and the corresponding average performance indicator  $K_i$  is illustrated in Fig. 14.

In Fig. 14, the aerodynamic performance of the staggered VAWT layout improves as the turbine spacing decreases and the inflow angle increases. Although the influence of rotation direction is relatively minor, the OED results indicate that the counter down configuration offers the best performance. Accordingly, the optimal layout combination, denoted as ExOpt, is identified as A1B3C2, corresponding to a turbine spacing of 1.5D, an inflow angle of 75°, and a counter down rotational configuration. This configuration provides the highest performance gain over two VAWTs operate independently.

It is worth noting that the ExOpt configuration is not among the nine predefined test cases in the orthogonal array. To assess its rationality, an additional simulation is performed to compute its performance indicator and verify the effectiveness of the proposed optimal layout. Although this combination lies at the boundary of the tested parameter space (i.e., the smallest spacing and the largest inflow angle), it reflects a local optimum within the current design range. Furthermore, two special layout configurations with variable turbine spacing (ranging from 1.5D to 2.5D) are considered for comparison: a parallel layout with an inflow angle of 90°, and a tandem layout with an inflow angle of 0°. The comparison results are shown in Fig. 15.

As shown in Fig. 15, the ExOpt layout achieves a performance indicator of 1.05, which is higher than all nine OED test cases (Ex1–Ex9), thereby confirming the effectiveness of the OED method employed in this study.

For the parallel layout, the performance indicator decreases as rotor spacing increases. At a spacing of 1.5D, the parallel configuration outperforms the staggered layout. However, when the spacing exceeds 1.5D, certain staggered configurations exhibit better performance. For

**Table 7**OED results of staggered bottom-fixed VAWTs.

Ex. No	A	В	С	$\Omega_1$	$\Omega_2$	Ω
Ex1	1	1	1	0.980	1.071	1.026
Ex2	1	2	2	1.011	1.078	1.044
Ex3	1	3	3	1.018	1.078	1.048
Ex4	2	2	3	1.002	1.066	1.034
Ex5	2	1	2	1.000	1.064	1.032
Ex6	2	3	1	1.030	1.059	1.044
Ex7	3	2	1	1.015	1.051	1.033
Ex8	3	3	2	1.027	1.045	1.036
Ex9	3	1	3	0.993	1.065	1.029
$K_1$	1.0393	1.0290	1.0343	_	_	-
$K_2$	1.0367	1.0370	1.0373	_	_	-
$K_3$	1.0327	1.0427	1.0370	-	-	-
R(μ)	0.0067	0.0137	0.0030	-	-	-

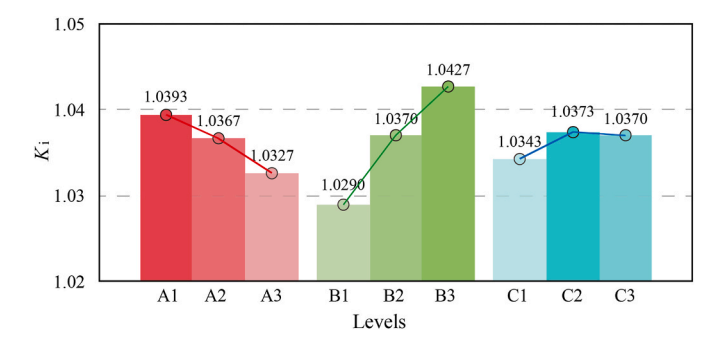


Fig. 14. Relationship between layout factors and average performance indicators (Ki).

example, Ex6 ( $\Omega=1.044$ ) outperforms the 2.0D parallel layout ( $\Omega=1.040$ ), and Ex8 ( $\Omega=1.036$ ) surpasses the 2.5D parallel layout ( $\Omega=1.034$ ).

In the case of tandem layouts, all tested configurations with varying turbines spacing yield performance indicators below 1, indicating a decline in overall wind farm performance due to strong wake interference affecting the downstream turbine.

### 4.1.3. Flow characteristics of staggered bottom-fixed VAWTs

To further reveal the flow mechanisms underlying the impact of different layout configurations on overall wind farm performance, the velocity fields corresponding to each layout scheme are computed and presented in Fig. 16.

As shown in Fig. 16a, a single isolated VAWT generates a clear downstream wake with reduced velocity and elevated turbulence intensity. Outside the wake centerline, rotor-induced momentum redistribution creates acceleration zones where local wind speeds exceed the freestream velocity.

In the tandem layout (Fig. 16c–e), placing VAWT2 directly behind VAWT1 results in reduced aerodynamic efficiency, with performance indicators below 1. VAWT2 operates within the low-velocity wake of VAWT1, generating little effective power while also negatively impacting the upstream rotor. This adverse interaction weakens as spacing increases. Compared to the isolated case, performance drops by 17.8 %, 8.3 %, and 6.4 % for inter-rotor distances of 1.5D, 2.0D, and 2.5D, respectively. The primary cause is the persistent low-speed wake from VAWT1, which limits flow recovery and reduces the overall performance of both turbines.

In contrast, both parallel and staggered layouts exhibit positive synergy effects ( $\Omega>1$ ), mainly due to partial wake overlap and mutual interference between the two VAWTs. These interactions promote faster flow recovery toward the freestream velocity. Under suitable layout conditions, a "jet-channeling" effect emerges between the wake regions (Fig. 16f–h), where the local velocity exceeds the surrounding wind speed. This phenomenon enhances the aerodynamic performance of both VAWT1 and VAWT2 in parallel and staggered configurations. Specifically:

(1) At a turbine spacing of 1.5D, the parallel layout outperforms the optimal staggered configuration (ExOpt) in terms of performance indicator, as shown in Fig. 16b and f. Compared to a single VAWT operating in isolation, the performance increases by 5.3 % for the parallel layout and 5.0 % for the ExOpt staggered layout. The superior performance of the parallel configuration is mainly due to the enhanced inflow conditions for VAWT2. Positioned directly beside and close to VAWT1, it benefits from the accelerated flow generated by the upstream rotor, resulting in a higher effective inflow velocity. Additionally, the parallel layout enables a more balanced distribution of the incoming wind between the two turbines, which helps reduce unsteady loading and

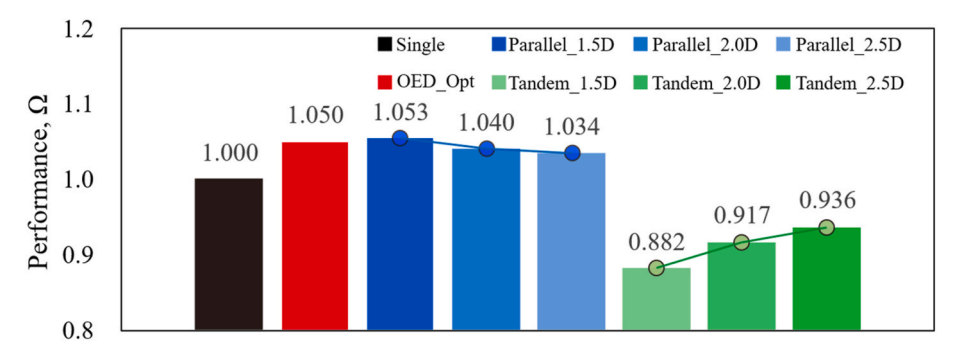


Fig. 15. Comparative analysis of performance indicators for VAWTs under parallel, tandem, and optimized staggered (ExOpt) layouts.

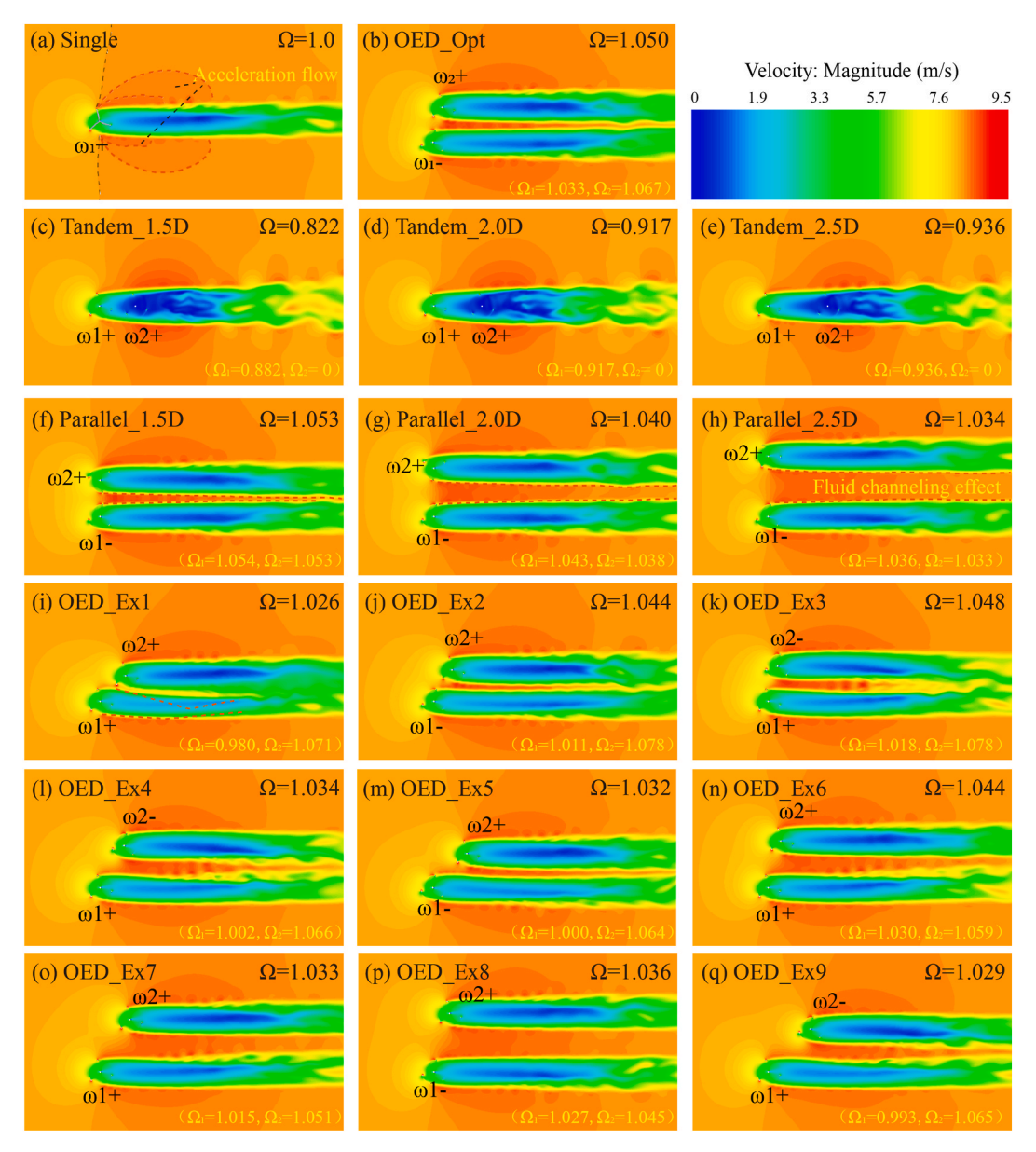


Fig. 16. Comparison of flow velocity contours for VAWTs under different layout configurations.

turbulence intensity, thereby improving aerodynamic efficiency. In contrast, under the same spacing, the staggered layout may introduce flow asymmetry or unstable wake interactions due to the lateral offset of VAWT2. This limits its ability to fully capture

- the upstream acceleration zone, slightly reducing its performance gain.
- (2) As the spacing between the two parallel VAWTs increases to 2.5D, the performance gain gradually diminishes (Fig. 16f-h). Compared to the isolated case, the performance indicators

increased by 5.3 %, 4.0 %, and 3.4 % at spacings of 1.5D, 2.0D, and 2.5D, respectively. This decline is mainly due to the reduced wake overlap at larger spacings, which weakens the flow recovery and wake restructuring effects. Additionally, the accelerated flow generated by VAWT1 has more time and space to dissipate before reaching VAWT2. As a result, the downstream turbine relies more on the undisturbed freestream rather than the favorable upstream acceleration, leading to a reduced aerodynamic benefit. Compared to the strong wake interaction and enhanced flow recovery observed at closer spacings, this natural restoration is insufficient to maintain the same level of performance improvement.

At turbine spacings of 2.0D and 2.5D, the staggered layout begins to outperform the parallel configuration. Due to the lateral offset of VAWT2, it is positioned closer to the acceleration zone generated by VAWT1 and can more effectively harness the available wind energy. For example, when the inflow angle is 75°, the performance indicators under the staggered layout reach 1.044 and 1.036 for 2.0D and 2.5D, respectively (Fig. 16n and p), compared to 1.040 and 1.034 under the parallel layout (Fig. 16g and h).

(3) When the rotor spacing is 2.0D or 2.5D and the inflow angle is less than 75°, the staggered layout yields lower performance indicators than the corresponding parallel configurations (Fig. 16i, m, and 16q). This is primarily because a smaller inflow angle positions VAWT2 closer to the direct downstream wake of VAWT1, exposing it to lower wind speeds and higher turbulence intensity. As a result, the staggered layout loses its advantage, as VAWT2 can neither avoid the wake nor benefit from the upstream flow acceleration. In addition, the presence of VAWT2 may deflect the wake of VAWT1 vertically (Fig. 16i), leading to more unstable upstream flow conditions, including asymmetric pressure distributions and increased turbulence. These effects ultimately degrade the aerodynamic performance of VAWT1.

# 4.2. Aero-hydrodynamic analysis of the staggered floating VAWTs

In Section 4.1, the optimization results for bottom-fixed VAWTs have shown that at small turbine spacing of 1.5D, parallel layouts generally exhibit better performance indicators than staggered configurations. However, for floating platforms with independent mooring systems, such tight is impractical due to the risk of platform collision and mooring line entanglement. Therefore, this study focuses on a more realistic offshore scenario where each VAWT is mounted on individual platform., and a spacing of 2.0D is selected to ensure operational safety and system stability.

Moreover, an inflow angle of  $\beta=60^\circ$  is adopted to enhance platform maneuverability under dynamic loading. and both VAWT1 and VAWT2 are set to rotate counterclockwise, as the rotation direction was previously shown to have limited influence on performance in staggered layouts. The layout parameters of staggered floating VAWTs are shown in Fig. 17. A corresponding bottom-fixed staggered VAWT with the identical parameters is also simulated to facilitate a fair comparison.

# 4.2.1. Aero-hydro coupled response

Fig. 18 illustrates the variation in torque coefficient over the final steady-state interval (330–360 s) for different layout configurations. As shown in Fig. 18a, the torque coefficient curve of a single isolated VAWT closely overlaps with that of VAWT1 in the fixed staggered layout, exhibiting a stable and periodic pattern over time. In contrast, VAWT2 shows a generally higher torque coefficient than the isolated case, due to the accelerated flow generated by VAWT1 (see Fig. 18b). The average torque coefficient of VAWT2 increases by 8.2 % compared to the single VAWT. Additionally, a noticeable phase lag is observed in the torque coefficient curve of VAWT2 relative to that of VAWT1 due to the initial

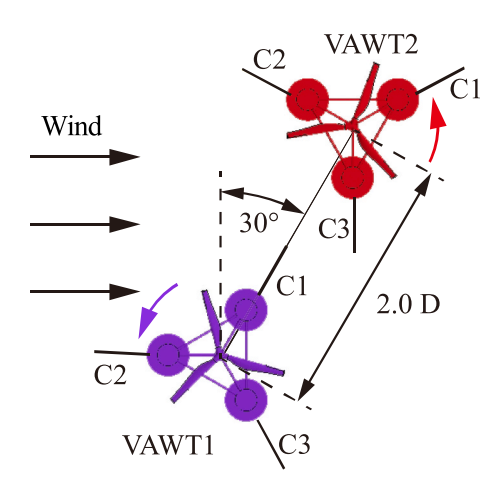


Fig. 17. Layout parameters of staggered floating VAWTs.

phase difference between the two VAWTs.

The floating VAWTs in staggered layout exhibit significantly higher instantaneous torque coefficients for both VAWT1 and VAWT2, primarily due to the platform's 6-DOF motion. Compared to their fixed counterparts at the same time instant, the floating VAWTs show increased torque peaks and more pronounced fluctuations.

By averaging the torque coefficients over the final 20 steady-state rotational revolutions, it is found that in the floating staggered configuration, the average torque coefficients of VAWT1 and VAWT2 increase by approximately 27 % and 24 %, respectively, relative to the single-isolated VAWT case. This indicates that the floating staggered layout offers stronger aerodynamic synergy than the fixed layout, further enhancing the overall wind farm performance.

To investigate the flow mechanisms underlying the improved performance of the floating staggered configuration, Fig. 19 compares the velocity fields and wake structures between the floating and fixed staggered VAWT layouts.

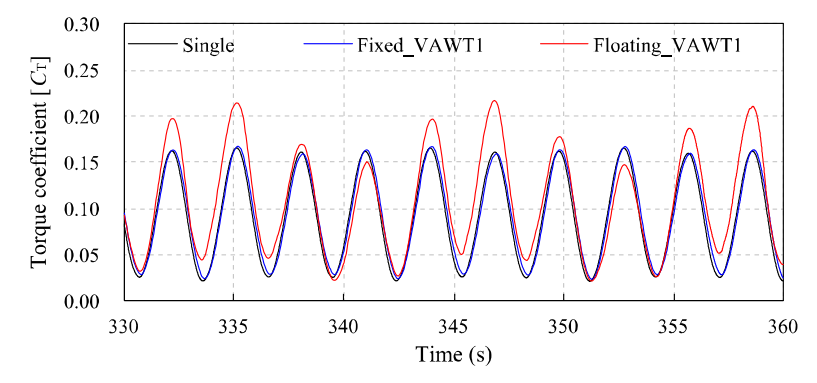
As shown in Fig. 19b, the fixed staggered VAWT layout exhibits significant velocity deficits in the wake region, with a large low-velocity zone forming downstream of the turbines along the positive X-direction, indicating substantial energy loss. In contrast, the floating staggered VAWT layout demonstrates much better wake recovery in the same region (Fig. 19a).

This improvement is primarily attributed to the platform motions induced by wave loads, which generate both translational and rotational displacements in horizontal and vertical directions. These 6-DOF responses enhance the interaction between the rotor wake and the surrounding freestream, promoting momentum exchange and energy entrainment. Moreover, the interaction and merging of the wakes from VAWT1 and VAWT2 intensify shear-layer development and turbulence mixing, thereby accelerating wake dissipation and flow recovery.

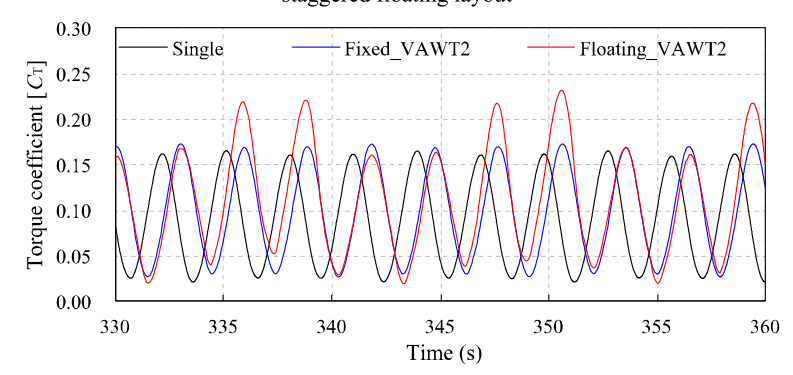
The 6-DOF dynamic responses of VAWT1 and VAWT2 in the floating staggered layout are illustrated in Fig. 20, representing the global motion of the overall center of mass of the rotor-platform system.

For the surge, pitch, and heave responses of the staggered floating VAWTs, both turbines show similar fluctuation amplitudes and response periods. This indicates that the primary platform motions governing the coupled aero-hydrodynamic behavior are not substantially affected by the 30° rotation of VAWT2. Because VAWT1 is positioned upstream, it encounters the incoming waves slightly earlier than VAWT2, leading to phase shifts and small differences in peak values.

This effect is further visualized in Fig. 21, which presents the instantaneous vortex structures and wave field characteristics at t=360 s. The wave crest reaches VAWT1 first, resulting in a significantly larger instantaneous pitch angle (1.83°) compared to VAWT2 (0.05°). The figure also shows mild wave run-up along the platform columns and the reorganization of wake vortices, confirming that platform—wave



(a) Torque coefficient of Single VAWT, VAWT1 in staggered bottom-fixed layout, and VAWT1 in staggered floating layout



(b) Torque coefficient of Single VAWT, VAWT2 in staggered bottom-fixed layout, and VAWT2 in staggered floating layout

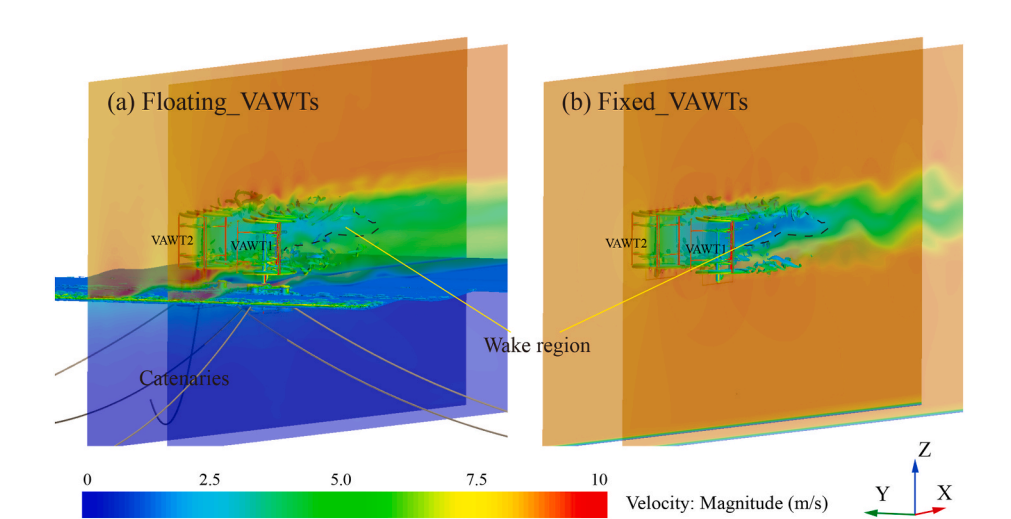


Fig. 18. Comparison of torque coefficients among different configurations.

Fig. 19. Comparison of velocity fields between floating and bottom-fixed staggered VAWT layouts.

interactions directly contribute to the phase differences observed in the global 6-DOF responses.

In contrast, VAWT2 shows slightly larger roll, yaw, and sway responses than VAWT1. This is mainly due to the different layouts of the two VAWTs and how their platforms react to wind and wave forces. VAWT1 uses a symmetric mooring system and a floating platform with even wave contact, which helps keep wave loads balanced. VAWT2's mooring system, however, is rotated 30° from its original direction, creating uneven tension and a restoring moment around the Y-axis that increases its side-to-side motion.

These structural and motion differences help explain why VAWT2, although placed in the accelerated wake of VAWT1, shows a smaller increase in torque coefficient compared to VAWT1 when measured against the isolated case, as observed in the torque coefficient results of Fig. 18. This highlights that while downstream turbines can benefit from wake acceleration, the platform's dynamic behavior may reduce some of the aerodynamic gains for VAWT2 individually, even though the overall staggered floating layout still demonstrates enhanced aerodynamic synergy compared to the fixed-base case.

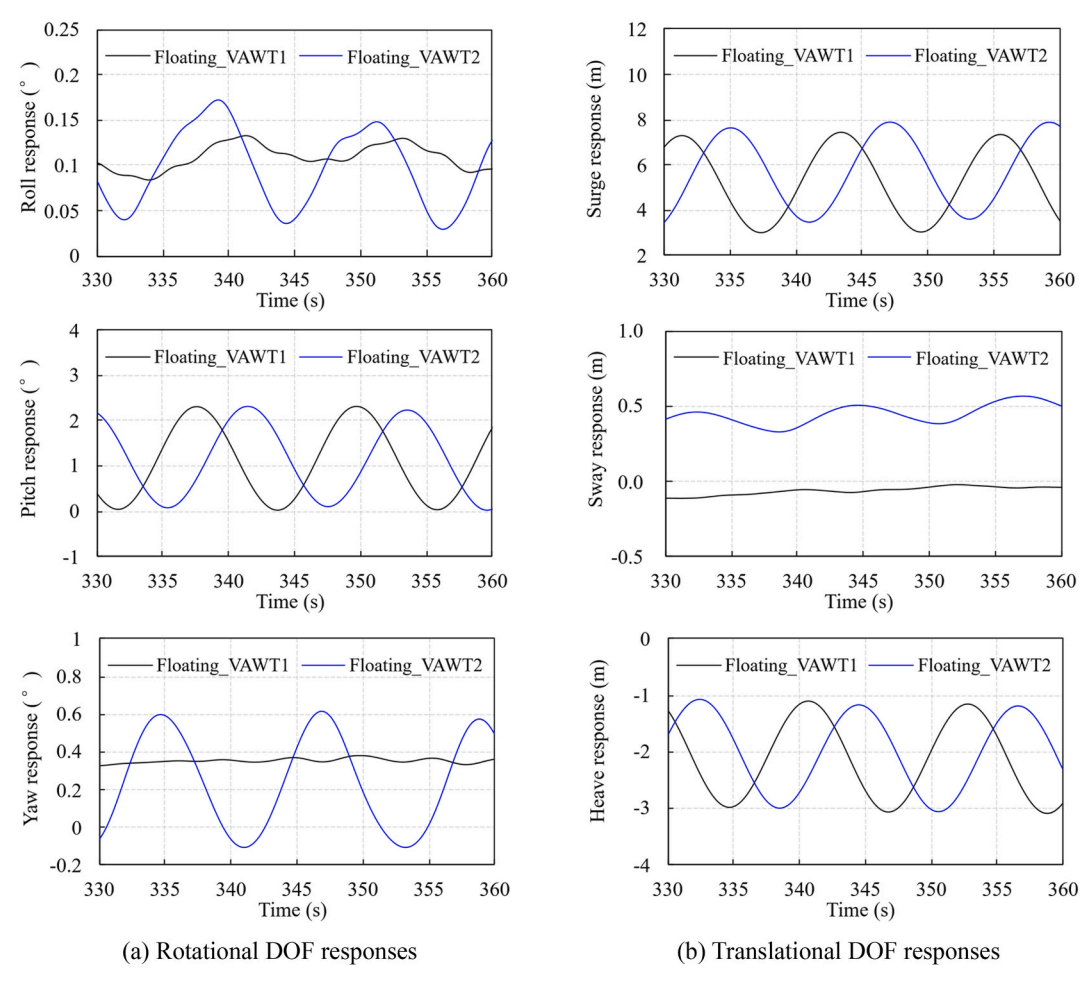
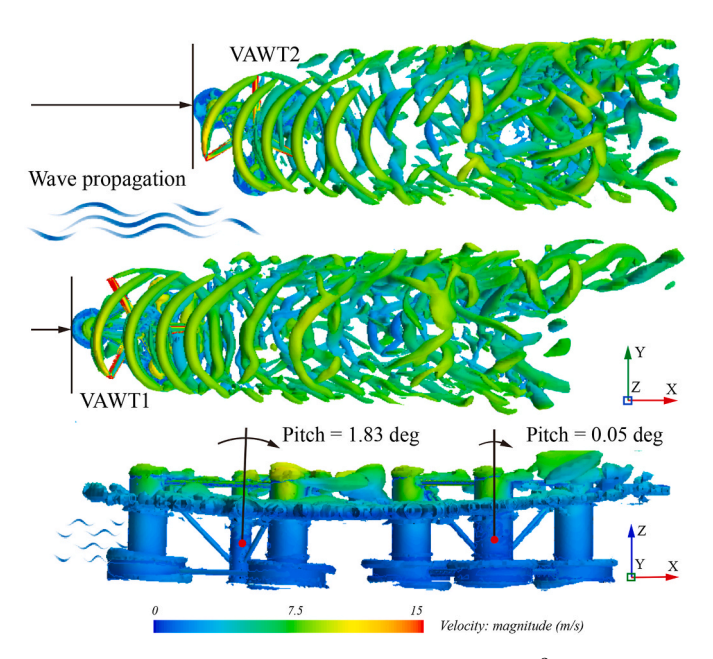


Fig. 20. Hydrodynamic responses of floating staggered VAWTs.



**Fig. 21.** Instantaneous Q-criterion isosurfaces ( $Q=0.01~s^{-2}$ ) colored by velocity magnitude at t=360~s for the floating staggered VAWT array: top view (upper) and front view (lower).

# 4.2.2. Flow characteristics of staggered floating VAWTs

Fig. 22 shows the time-averaged velocity fields and turbulent kinetic energy (TKE) distributions at  $Z=66\,\mathrm{m}$ , corresponding to the rotor midspan, for three cases: a single isolated VAWT, as well as the floating and fixed staggered VAWT layouts.

As shown in Fig. 22a-c, clear velocity deficits form downstream of the rotor during VAWT operation due to wind energy extraction. As the wake develops, mixing between the low-speed wake and the surrounding freestream gradually restores the flow.

Beyond  $X/D \geq 4$ , wake recovery varies noticeably across the three configurations:

- (1) Compared to the single isolated case, the staggered layout generates a channeling effect between the two VAWTs, accelerating the flow in this region. This effect is stronger in the floating staggered layout, where wake-side acceleration is more evident. The high-speed flow region is considerably larger than in either the fixed staggered or single-turbine case.
- (2) The performance indicator  $\Omega$  increases by 22 % in the floating staggered layout compared to the isolated case, while the fixed staggered layout shows a smaller increase of 3.7 %. This suggests that platform motion enhances aerodynamic synergy more effectively than a fixed-base configuration. This phenomenon has also been reported by Chen et al. [65], who numerically investigated the impact of pitch angle variation on twin VAWTs in a staggered layout. It was found that the pitch motion could accelerate the flow field between turbines and suppress the wake width, thus improving overall aerodynamic performance.

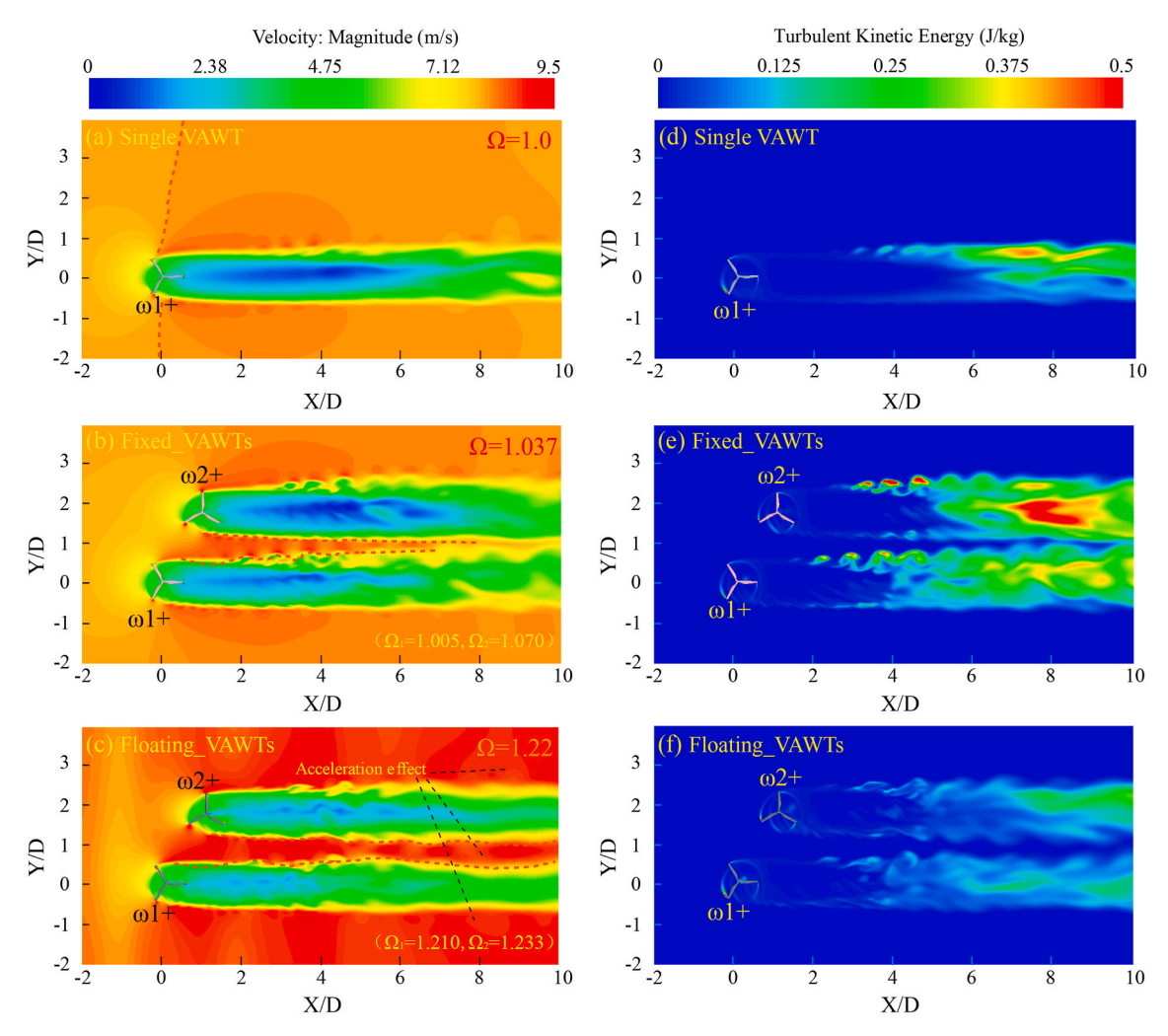


Fig. 22. Comparison of velocity field and turbulence kinetic energy distribution among floating staggered VAWTs, bottom-fixed staggered VAWTs, and a single VAWT.

In Fig. 22d–f, TKE levels are nearly depleted before the airflow reaches the rotor, due to the low inlet turbulence intensity (1 %). After interacting with the rotating blades and the floating platform, local turbulence levels rise significantly, particularly near the trailing edge of VAWT blades and around the turbine tower.

As the wake develops downstream, TKE increases rapidly. In the fixed staggered layout, wake–wake interactions between VAWT1 and VAWT2 lead to significantly higher TKE levels in the far wake region ( $6 \le X/D \le 10$ ) compared to the single VAWT case. In contrast, the floating staggered layout shows lower TKE levels beyond  $X/D \ge 8$ , indicating faster wake dissipation and earlier flow recovery. These results can be attributed to the platform's 6-DOF motion, which disrupts the coherent wake structures and promotes more effective turbulent mixing.

# 4.2.3. Wake structure evolution

To further quantify wake recovery across different VAWT layout schemes, the non-dimensional velocity  $U/U_{\infty}$  in the wake region is monitored at the rotor mid-span plane, as shown in Fig. 23.

As shown in Fig. 23, at the near-wake region (X/D=2), all layout schemes show the lowest velocity along the rotor centerline. Moving vertically away from the center, the velocity gradually increases, forming a bowl-shaped distribution that is approximately symmetrical about Y/D=0. Beyond X/D=2 (Fig. 23b-d), the symmetry of the velocity profile begins to break down. The wake shifts away from the rotor axis, and the asymmetry becomes more pronounced with increasing

downstream distance.

In staggered layouts, the wake of VAWT1 is influenced by the presence of VAWT2. In the far wake, the wake interaction promoting faster wake dissipation for VAWT1 compared to the single VAWT case. This effect is more significant in the floating staggered layout, where platform motion further accelerates wake recovery. By At X/D=4, the velocity deficit behind VAWT1 is nearly eliminated. As a result, VAWT1 shows higher wake velocities in the staggered layouts than in the single VAWT case, especially at X/D=4 and X/D=6. The flow channeling effect also increases the velocity above the rotor centerline. At Y/D=0.4, the velocity increases by 119 % and 182 % at X/D=4 and 6 in the floating staggered layout, and by 38 % and 69 % in the fixed staggered layout, respectively, compared to the isolated turbine.

At X/D=8, the flow channeling effect observed in the fixed staggered layout begins to weaken, and the wakes from both turbines start to merge. Compared to the fixed case, the floating staggered layout shows longer wake extension along the rotor centerline for both VAWTs. As a result, the velocity at the centerline is slightly lower, comparable to the isolated case. However, due to the narrower wake from VAWT1 in the floating setup, the velocity on both sides of the centerline remains higher than in the isolated and fixed configurations.

For VAWT2, the fixed staggered layout produces a wider velocity deficit region than the isolated case, particularly in the range of  $\rm X/D=3$  to 5. This is because VAWT2 sits downstream and slightly below VAWT1, drawing in low-speed flow from the edge of VAWT1's far wake. By  $\rm X/D=8$ , the fixed layout contains a large amount of high-TKE fluid,

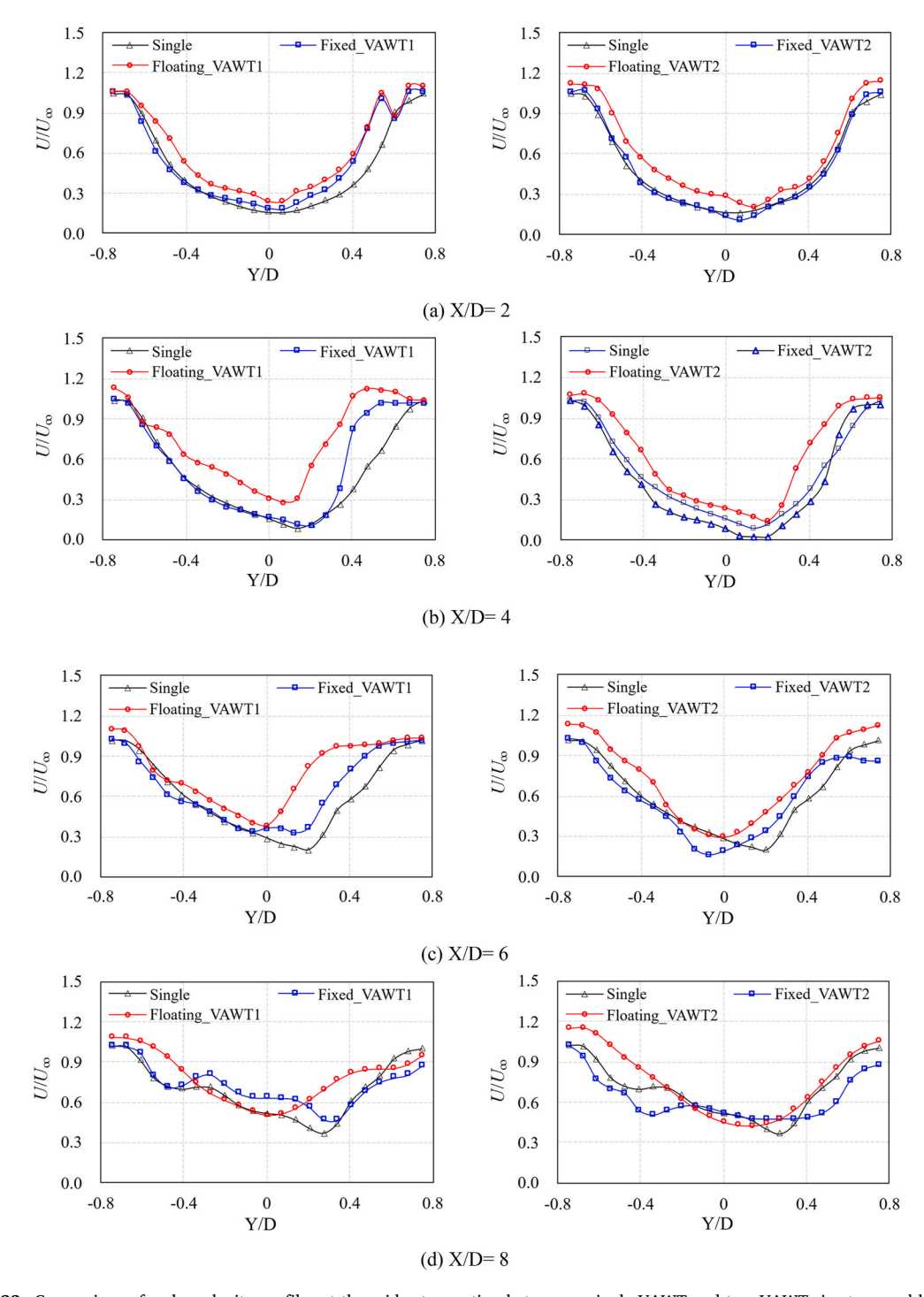


Fig. 23. Comparison of wake velocity profiles at the mid-rotor section between a single VAWT and two VAWTs in staggered layout.

increasing unsteadiness and causing lower flow velocity around VAWT2 compared to the isolated configuration.

In the range of  $2{\le}X/D \le 6$ , the floating staggered layout consistently shows better wake recovery than both the fixed layout and the isolated case, with higher velocities along the rotor centerline. Only at X/D=8 does the centerline velocity become slightly lower than the other two layouts. This reduction is similar to the behavior observed for VAWT2 and is mainly due to the influence of platform motion. While the motion enhances overall dissipation, the low-speed fluid in the wake tends to retain the upstream flow pattern. The additional acceleration introduced by the platform leads to distinct wake behavior that differs from the more stable pattern seen in fixed layouts.

To better understand the effect of fluid channeling on the wake characteristics of each VAWT in the staggered layout, Fig. 24 shows the velocity monitoring points (marked in red) distributed along the fluid channel between the two VAWTs. For comparison, the same monitoring locations are also applied to the single VAWT configuration, as shown in Fig. 24a.

These monitor points are used to extract the streamwise evolution of the wake velocity along the centerline for quantitative comparison, as shown in Fig. 25.

As shown in Fig. 25, within the range of  $X/D \le 4$ , the flow velocity in the channel region between the turbines is significantly higher in both staggered layouts compared to the single VAWT case. However, as the

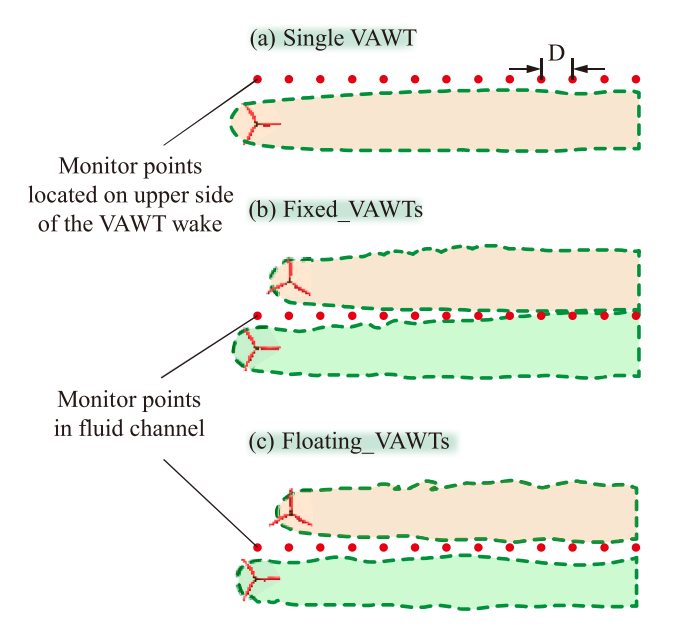


Fig. 24. Monitoring point distribution in the wake and inter-wake channel of VAWTs.

distance increases beyond  $X/D \geq 4$ , the wake from the floating VAWTs dissipates more rapidly due to platform motion, weakening the flow channeling effect.

Between X/D =5 and 7, the platform motions in the floating staggered layout enhance shear-layer instability and promote earlier wake mixing, which draws more high-momentum flow into the inter-wake channel. This yields higher centerline velocities compared to the single-VAWT case. Beyond X/D =8 the earlier momentum replenishment reduces downstream velocity gradients, leading to lower TKE levels than in the fixed staggered layout while maintaining higher mean velocities.

In contrast, the fixed staggered layout confines the flow acceleration effect to a narrow region directly behind the rotors. With increasing distance, natural diffusion and energy loss cause this effect to diminish, disappearing almost completely beyond X/D=6. Additionally, the influence of VAWT2's wake leads to increased mixing of low-energy fluid in the far wake. This results in a sharp rise in TKE at  $X/D \geq 8$ , increasing flow instability. Therefore, in the fixed staggered layout, the velocity in the channel can be either higher or lower than the single VAWT case.

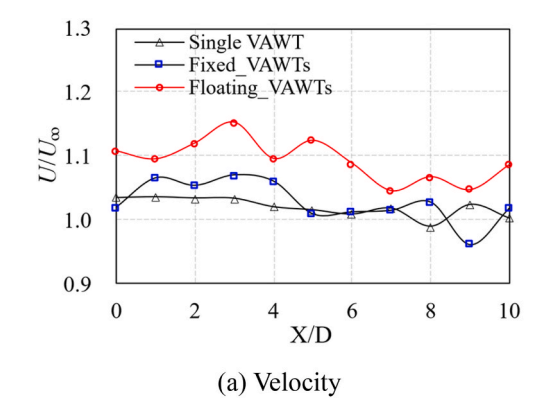
# 5. Conclusions

This study presents a fully coupled aero-hydro analysis of staggered floating VAWTs using the DFBI approach in STAR-CCM+. The work

begins by applying an OED method to optimize the staggered layout parameters of bottom-fixed VAWTs, and then compares their performance with parallel and tandem configurations. Based on these findings, the feasibility and potential advantages of using staggered layouts for floating VAWTs are investigated. The main conclusions are summarized as follows:

- (1) The OED results show that among the three layout parameters, the inflow angle has the strongest influence, followed by the turbine spacing, while the rotation direction has the least impact. The optimal layout configuration (ExOpt) consists of a turbine spacing of 1.5D, an inflow angle of 75°, and a counter-down rotation (i.e., opposite rotation aligned with the flow direction). This layout yields a performance indicator of  $\Omega=1.050$ , representing a 5 % increase in power output compared to two single VAWTs operating independently.
- (2) A detailed comparison among tandem, parallel, and staggered layouts was conducted across different turbine spacings. For tandem configurations, the downstream turbine operates directly in the wake of the upstream one, resulting in a severe loss of available wind energy and a noticeable performance drop of up to 17.8 %. In contrast, parallel layouts with small spacing (1.5D) benefit from the overlap of accelerated flows between turbines, achieving the highest performance indicator ( $\Omega = 1.053$ ) among all cases. However, as turbine spacing increases, the interaction between wakes weakens due to natural dissipation, and the performance advantage of parallel layouts diminishes. In these cases, staggered layouts become more effective, particularly because the second VAWT is positioned closer to the high-speed recovery region behind the first VAWT. This configuration allows more efficient wind energy utilization and helps maintain higher performance across a wider range of turbine spacings.
- (3) A fully coupled simulation of staggered floating VAWTs was carried out to evaluate the impact of platform motion. The results show that the 6-DOF response of the floating system enhances both wake dissipation and the formation of high-speed flow channels between turbines wakes. Compared to the single VAWT case, the floating staggered layout achieved a performance indicator of  $\Omega=1.22$ , representing a 22 % performance gain, while the corresponding fixed-bottom staggered layout only reached  $\Omega=1.037$ . The average torque coefficients of the two floating VAWTs also increased by approximately 27 % and 24 %, respectively. These improvements are closely linked to the interaction between platform motion and turbulent wake structures, leading to accelerated energy recovery in the downstream region.

The findings of this study provide useful guidance for the practical layout of floating VAWTs in offshore wind farms. For configurations



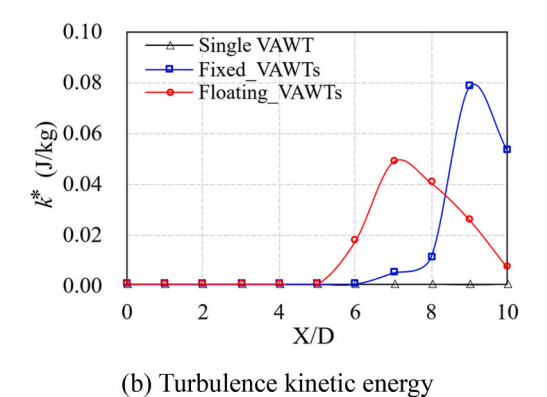


Fig. 25. Comparsion of velocity and turbulence kinetic energy in the wake and inter-wake channel of staggered VAWTs.

where two VAWTs are installed on a shared platform, a parallel layout with a spacing of 1.5D is recommended due to its strong performance and compact design. On the other hand, if each VAWT is mounted on an independent floating platform, a staggered layout with larger spacing ( $\geq$ 2.0D) is preferred, not only for better aerodynamic performance, but also to reduce the risk of mooring line entanglement and physical collision between platforms.

In future large-scale deployments, floating VAWT farms are likely to face design challenges involving complex wake interactions, platform dynamics, and mooring loads. This work lays a foundation for addressing such challenges by highlighting the aerodynamic synergy mechanisms and motion-induced benefits of staggered layouts. Further research is encouraged to extend the current layout optimization strategy to arrays involving more than two turbines, where wake interactions are more nonlinear and configuration-sensitive. Future studies may also focus on the aerodynamic and hydrodynamic performance of floating VAWTs under irregular wave conditions, explore the influence of alternative rotor designs (e.g.,  $\Phi$ -shaped blades), and evaluate the feasibility of novel shared-platform configurations in staggered or array layouts.

Moreover, in floating configurations with 6-DOF platform motions and in non-uniform inflows such as sheared wind, the mirror symmetry between clockwise and counterclockwise co-rotating cases may be broken. Future work will therefore include a more detailed investigation of co-rotating clockwise/counterclockwise scenarios under realistic offshore conditions.

### CRediT authorship contribution statement

Qingsong Liu: Writing – original draft, Visualization, Validation, Methodology, Investigation, Conceptualization. Haoda Huang: Writing – original draft, Visualization, Investigation. Gregorio Iglesias: Writing – review & editing, Supervision, Conceptualization. Jin Wang: Writing – review & editing, Software, Resources. Musa Bashir: Writing – review & editing, Supervision, Project administration.

# Declaration of competing interest

The authors declare that they have no known competing financial interests or personal relationships that could have appeared to influence the work reported in this paper.

# Acknowledgements

This research is funded by UKRI Innovate UK under grant numbers TS/Y006364/1, TS/Y005236/1, and TS/X018407/1. The authors gratefully acknowledge the support of the High-Performance Computer Cluster at Liverpool John Moores University (LJMU) for generously providing the computational resources for this research.

# Data availability

No data was used for the research described in the article.

# References

- [1] Global Wind Energy Council. Global wind report 2025. Lisbon: GWEC; 2025.
- [2] Ghigo A, Faraggiana E, Giorgi G, et al. Floating Vertical Axis Wind Turbines for offshore applications among potentialities and challenges: A review. Renew Sustain Energy Rev 2024;193:114302.
- [3] Aslam Bhutta M, Hayat N, Farooq A, et al. Vertical axis wind turbine A review of various configurations and design techniques. Renew Sustain Energy Rev 2012;16 (4):1926–39.
- [4] Borg M, Collu M, Kolios A. Offshore floating vertical axis wind turbines, dynamics modelling state of the art. Part II: Mooring line and structural dynamics. Renew Sustain Energy Rev 2014;39:1226–34.
- [5] Cho S, Choi M, Gao Z, et al. Fault detection and diagnosis of a blade pitch system in a floating wind turbine based on Kalman filters and artificial neural networks. Renew Energy 2021;169:1–13.

[6] Kang J, Sun L, Soares CG. Fault Tree Analysis of floating offshore wind turbines. Renew Energy 2019;133:1455–67.

- [7] Li JW, Bian JY, Chuang ZJ, et al. Impact of pitch actuator fault on 10-MW semisubmersible floating wind turbine. Ocean Eng 2022;254:111375.
- [8] Lin JH, Wang YW, Duan HW, et al. A scaled wind turbine model-based aerodynamic testing apparatus for offshore floating wind turbines. Journal of Marine Engineering and Technology 2023;22(6):263–72.
- [9] Li H, Soares CG. Assessment of failure rates and reliability of floating offshore wind turbines. Reliab Eng Syst Saf 2022;228:108777.
- [10] Chitteth Ramachandran R, Desmond C, Judge F, et al. Floating wind turbines: Marine operations challenges and opportunities. Wind Energy Science 2022;7(2): 903-24
- [11] Liu T, Halse KH, Leira BJ, et al. Comparative study of the mating process for a spartype floating wind turbine using two alternative installation vessels. Appl Ocean Res 2023;132:103452.
- [12] McMorland J, Collu M, McMillan D, Carroll J. Operation and maintenance for floating wind turbines: A review. Renew Sustain Energy Rev 2022;163:112499.
- [13] Hand B, Kelly G, Cashman A. Aerodynamic design and performance parameters of a lift-type vertical axis wind turbine: A comprehensive review. Renew Sustain Energy Rev 2021;139:110699.
- [14] Griffith DT, Barone M, Paquette J, et al. Design studies for deep-water floating offshore vertical axis wind turbines. United States: Office of Scientific and Technical Information Technical Reports 2018: 30-31.
- [15] Ennis BL, Griffith DT. System levelized cost of energy analysis for floating offshore vertical-axis wind turbines. United States: Office of Scientific and Technical Information Technical Reports 2018: 71-72.
- [16] Borg M, Collu M, Brennan F. Offshore floating vertical axis wind turbines: Advantages, disadvantages, and dynamics modelling state of the art. Marine and offshore renewable energy conference. London: The Royal Institution of Naval Architects; 2012.
- [17] Dabiri JO. Potential order-of-magnitude enhancement of wind farm power density via counter-rotating vertical-axis wind turbine arrays. J Renew Sustain Energy 2011;3:043104.
- [18] Shaheen M, Abdallah S. Development of efficient vertical axis wind turbine clustered farms. Renew Sustain Energy Rev 2016;63:237–44.
- [19] Rajagopalan RG, Rickerl TL, Klimas PC. Aerodynamic interference of vertical axis wind turbines. J Propul Power 1990;6(5):645–53.
- [20] Hansen JT, Mahak M, Tzanakis I. Numerical modelling and optimization of vertical axis wind turbine pairs: A scale up approach. Renew Energy 2021;171:1371–81.
- [21] Whittlesey RW, Liska S, Dabiri JO. Fish schooling as a basis for vertical axis wind turbine farm design. Bioinspiration Biomimetics 2010;5:035005.
- [22] Vergaerde A, Troyer TD, Muggiasca S, et al. Experimental characterisation of the wake behind paired vertical-axis wind turbines. J Wind Eng Ind Aerod 2020;206: 104353.
- [23] Shen WZ, Zhang JH, Sørensen JN. Actuator surface model for wind turbine flow computations. 2007 European wind energy conference and exhibition. Milan, Italy: Proceedings of European wind energy conference 2007. 2007.
- [24] Riva L, Giljarhus KE, Hjertager B, et al. Implementation and application of the actuator line model by OpenFOAM for a vertical axis wind turbine. Mater Sci Eng 2017;276:012002.
- [25] Bremseth J, Duraisamy K. Computational analysis of vertical axis wind turbine arrays. Theor Comput Fluid Dynam 2016;30(5):387–401.
- [26] Silva JE, Danao LAM. Varying VAWT cluster configuration and the effect on individual rotor and overall cluster performance. Energies 2021;14(6):1567.
- [27] Lam HF, Peng HY. Measurements of the wake characteristics of co- and counterrotating twin H-rotor vertical axis wind turbines. Energy 2017;131(15):13–26.
- [28] Schatzle PR, Klimas PC, Spahr HR. Aerodynamic interference between two Darrieus wind turbines. J Energy 1981;5(2):84–8.
- [29] Rajagopalan RG, Rickerl TL, Klimas PC. Aerodynamic interference of vertical axis wind turbines. J Propul Power 1990;6(5):645–53.
- [30] Zanforlin S, Nishino T. Fluid dynamic mechanisms of enhanced power generation by closely spaced vertical Axis wind turbines. Renew Energy 2016;99:1213–26.
- [31] Shaheen M, El-Sayed M, Abdallah S. Numerical study of two-bucket Savonius wind turbine cluster. J Wind Eng Ind Aerod 2015;137:78–89.
- [32] Sahebzadeh S, Rezaeiha A, Montazeri H. Vertical-axis wind-turbine farm design: Impact of rotor setting and relative arrangement on aerodynamic performance of double rotor arrays. Energy Rep 2022;8:5793–819.
- [33] Thomas RN. Coupled vortex vertical axis wind turbine: US6784566B2. 2004.
- [34] Alexander AS, Santhanakrishnan A. Mechanisms of power augmentation in two side-by-side vertical axis wind turbines. Renew Energy 2020;148:600–10.
- [35] Chen WH, Chen CY, Huang CY, et al. Power output analysis and optimization of two straight-bladed vertical-axis wind turbines. Appl Energy 2017;185:223–32.
- [36] Shaheen M, Abdallah S. Efficient clusters and patterned farms for Darrieus wind turbines. Sustain Energy Technol Assessments 2017;19:125–35.
- [37] Sun XJ, Luo DH, Huang DG, et al. Numerical study on coupling effects among multiple Savonius turbines. J Renew Sustain Energy 2012;4(5):053107.
- [38] Jang C, Kim Y, Kang S, et al. An experiment for the effects of the distance and rotational direction of two neighboring vertical Savonius blades. Int J Energy Res 2016;40(5):632–8.
- [39] Ahmadi-Baloutaki M, Carriveau R, Ting SD. A wind tunnel study on the aerodynamic interaction of vertical axis wind turbines in array configurations. Renew Energy 2016;96:904–13.
- [40] Shaheen M, Abdallah S. Efficient clusters and patterned farms for Darrieus wind turbines. Sustain Energy Technol Assessments 2017;19:125–35.

- [41] Xu Z, Chen J, Li C, et al. Research on the adaptability of dynamic pitch control strategies on H-type VAWT close-range arrays by simulation study. Renew Energy 2023;218:119231.
- [42] Zheng HD, Zheng XY, Zhao SX. Arrangement of clustered straight-bladed wind turbines. Energy 2020;200:117563.
- [43] Yutaka H, Yoshifumi J, Tomoyuki O, et al. Numerical analysis of the dynamic interaction between two closely spaced vertical-axis wind turbines. Energies 2021; 14(8):2286.
- [44] Yutaka H, Yoshifumi J, Shu Y, et al. Numerical simulation on tandem layout of two vertical axis wind turbines. Proceedings of the 2019 annual general meeting, vol. 10. Akita, Japan: JSME; 2019.
- [45] Sadra S, Abdolrahim R, Hamid M. Towards optimal layout design of vertical-axis wind-turbine farms: double rotor arrangements. Energy Convers Manag 2020;226: 113527
- [46] Zhang DQ, Liu ZQ, Li WP. LES simulation study of wind turbine aerodynamic characteristics with fluid-structure interaction analysis considering blade and tower flexibility. Energy 2023;282:128840.
- [47] Giorgetti S, Pellegrini G, Zanforlin S. CFD investigation on the aerodynamic interferences between medium-solidity Darrieus Vertical Axis Wind Turbines. Energy Proc 2015;81:227–39.
- [48] Tavernier DD, Ferreira C, Li A, et al. Towards the understanding of vertical-axis wind turbines in double-rotor configuration. Journal of physics: Conference series, 1037. Shanghai, China: IOP Publishing; 2018, 022015.
- [49] Bangga G, Lutz T, Krämer E. Energy assessment of two vertical axis wind turbines in side-by-side arrangement. J Renew Sustain Energy 2018;10(3):033303.
- [50] Bastankhah M, Porté-Agel F. Wind farm power optimization via yaw angle control: A wind tunnel study. J Renew Sustain Energy 2019;11:023301.
- [51] Miao W, Li C, Yang J, et al. Numerical investigation of the yawed wake and its effects on the downstream wind turbine. J Renew Sustain Energy 2016;8:033303.
- [52] Rosenberg A, Selvaraj S, Sharma A. A novel dual-rotor turbine for increased wind energy capture. J Phys Conf 2014;524:012078.

- [53] Zhang Y, Cai X, Lin S, et al. CFD simulation of Co-planar multi-rotor wind turbine aerodynamic performance based on ALM method. Energies 2022;15:6422.
- [54] Zhang Z, Kuang L, Zhao Y, et al. Numerical investigation of the aerodynamic and wake characteristics of a floating twin-rotor wind turbine under surge motion. Energy Convers Manag 2023;283:116957.
- [55] Zhang Z, Yang H, Zhao Y, et al. A novel wake control strategy for a twin-rotor floating wind turbine: Mitigating wake effect. Energy 2024;287:129619.
- [56] Veritas DN. Environmental conditions and environmental loads. Recommended Practice DNV-RP-C205; 2007.
- [57] Choi J, Bum Yoon S. Numerical simulations using momentum source wave-maker applied to RANS equation model. Coast Eng 2009;56(10):1043–60.
- [58] Liu Q, Bashir M, Iglesias G, et al. Investigation of aero-hydro-elastic-mooring behavior of a H-type floating vertical axis wind turbine using coupled CFD-FEM method. Appl Energy 2024;372:123816.
- [59] Liu Q, Bashir M, Huang H, et al. Nature-inspired innovative platform designs for optimized performance of Floating vertical Axis wind turbines. Appl Energy 2025; 380:125120.
- [60] Robertson A, Jonkman J, Masciola M, et al. Definition of the semisubmersible floating system for phase II of OC4. United States: Office of scientific and technical information reports. 2014.
- [61] Buoyweather. Global marine weather forecasts and wave data. https://www.buoyweather.com/#6/50.25/-0.7/SWELL. [Accessed 19 April 2025].
- [62] Jiao J, Chen Z, Chen S, et al. Ship hydroelasticity responses in long-crested irregular waves by CFD-FEM simulation in comparison with segmented model experiment. Ocean Eng 2025;326:120886.
- [63] Romanowski A, Tezdogan T, Turan O. Development of a CFD methodology for the numerical simulation of irregular sea-states. Ocean Eng 2019;192:106530.
- [64] Hu L, Yuan Z, Liu J, et al. 3-DOF motion response analysis of damaged ships in quartering waves. Appl Ocean Res 2025;161:104659.
- [65] Chen Y, Kuang L, Su J, et al. Investigation of pitch angles on the aerodynamics of twin-VAWT under staggered arrangement. Ocean Eng 2022;254:111385.